HHS Public Access

Author manuscript

Nat Methods. Author manuscript; available in PMC 2024 April 12.

Published in final edited form as:

Nat Methods. 2023 November ; 20(11): 1802–1809. doi:10.1038/s41592-023-02020-9.

Fatigue-resistant hydrogel optical fiber enables peripheral nerve optogenetics during locomotion

Xinyue Liu[1,2], **Siyuan Rao**[3], **Weixuan Chen**[3], **Kayla Felix**[3], **Jiahua Ni**[1], **Atharva Sahasrabudhe**[4,5,6], **Shaoting Lin**[1,7], **Qianbin Wang**[3], **Yuanyuan Liu**[8], **Zhigang He**[9,10], **Jingyi Xu**[3], **Sizhe Huang**[3], **Eunji Hong**[3], **Todd Yau**[11], **Polina Anikeeva**[4,5,12,13], **Xuanhe Zhao**[1,14]

[1] Department of Mechanical Engineering, Massachusetts Institute of Technology, Cambridge, MA, USA.

[2] Department of Chemical Engineering and Materials Science, Michigan State University, East Lansing, MI, USA.

[3] Department of Biomedical Engineering, University of Massachusetts Amherst, Amherst, MA, USA.

[4] Research Laboratory of Electronics, Massachusetts Institute of Technology, Cambridge, MA, USA.

[5] McGovern Institute for Brain Research, Massachusetts Institute of Technology, Cambridge, MA, USA.

[6] Department of Chemistry, Massachusetts Institute of Technology, Cambridge, MA, USA.

[7] Department of Mechanical Engineering, Michigan State University, East Lansing, MI, USA.

[8] Somatosensation and Pain Unit, National Institute of Dental and Craniofacial Research, National Center for Complementary and Integrative Health, National Institute of Health, Bethesda, MD, USA.

[9] F.M. Kirby Neurobiology Center, Boston Children's Hospital, Harvard Medical School, Boston, MA, USA

[10] Department of Neurology, Harvard Medical School, Boston, MA, USA

[11] Department of Biochemistry and Molecular Biology, University of Massachusetts Amherst, Amherst, MA, USA

liuxin58@msu.edu, syrao@umass.edu, anikeeva@mit.edu, zhaox@mit.edu.

These authors contributed equally: Xinyue Liu, Siyuan Rao.

Author Contributions

These authors contributed equally: Polina Anikeeva, Xuanhe Zhao. X.L., S.R., P.A. and X.Z. discussed the initial concept of the hydrogel optical fibers. X.L., S.R., S.L. and S. H. designed the materials and fabrication methods for the hydrogel optical fibers. X.L., J.N. and S.L. designed and conducted the characterization of materials and devices and data analysis. X.L., S.R., W.C., A.S., Q.W. and E.H. conducted the in vivo and ex vivo experiments and data analysis. X.L., S.R., K.F., W.C., J.X., Y.L., Z.H., J.X. and T.Y. designed the behavior assays and conducted the behavioral analysis. X.L., S.R., P.A. and X.Z. wrote the manuscript with input from all authors.

Competing Interests

P.A. has a financial interest in NeuroBionics Inc., a biotechnology company focused on the development of multifunctional fibers for research and clinical applications. X.Z. has a financial interest in SanaHeal, a biotechnology company focused on the development of medical devices for surgical sealing and repair. Z.H. is an advisor of Myro Therapeutics, Axonis and Rugen Therapeutics. The remaining authors declare no competing interests.

[12] Department of Materials Science and Engineering, Massachusetts Institute of Technology, Cambridge, MA, USA.

[13] Department of Brain and Cognitive Sciences, Massachusetts Institute of Technology, Cambridge, MA, USA.

[14] Department of Civil and Environmental Engineering, Massachusetts Institute of Technology, Cambridge, MA, USA

Abstract

We develop soft and stretchable fatigue-resistant hydrogel optical fibers that enable optogenetic modulation of peripheral nerves in naturally behaving animals during persistent locomotion. The formation of polymeric nanocrystalline domains within the hydrogels yields fibers with low optical losses of 1.07 dB cm^{-1}, Young's modulus of 1.6 MPa, stretchability of 200%, and fatigue strength of 1.4 MPa against 30,000 stretch cycles. The hydrogel fibers permitted light delivery to the sciatic nerve, optogenetically activating hindlimb muscles in Thy1::ChR2 mice during 6-week voluntary wheel running assays while experiencing repeated deformation. The fibers additionally enabled optical inhibition of pain hypersensitivity in an inflammatory model in TRPV1::NpHR mice over an eight-week period. Our hydrogel fibers offer a motion-adaptable and robust solution to peripheral nerve optogenetics, facilitating the investigation of somatosensation with implications in motor recovery and pain management.

Optogenetics has transformed the field of systems neuroscience by providing a powerful tool that allows precise control over the activity of specific cell populations[1,2]. While it is routinely applied to the study of brain circuits, the applications of optogenetic modulation to peripheral nerves that undergo vigorous motion remain challenging (Figure 1a,b)[3,4]. Light delivery devices composed of rigid materials, such as silica fibers with GPa moduli can damage soft tissues with moduli in kPa-MPa range upon repeated deformation and displacement[5,6]. Additionally, implanting rigid devices within extremities may impede natural animal behaviors. Although flexible devices with microscale light-emitting diodes created through microfabrication are suitable for stimulating peripheral nerves and the spinal cord in freely moving rodents, their sophisticated design presents implementation challenges outside of specialized facilities[7–10]. More notably, vigorous and repeated deformation during locomotion may accelerate fatigue failures at rigid-soft interfaces within microfabricated devices, resulting in reduced efficacy and reliability of neuromodulation over time[11].

Optical fibers offer precise spatial targeting, scalable manufacturing, and facile coupling to commercial light sources[12–14]. Fibers composed of polymers, such as polycarbonate (PC), polymethyl methacrylate (PMMA), polystyrene (PS), and cyclic olefin copolymer (COC), enabled optogenetic stimulation in the mouse gut lumen and spinal cord[14,15]. However, the moduli in the GPa range and limited elasticity have hindered applications of polymer fibers in peripheral nerves experiencing large deformations (Extended Data Figure 1a,b)[3,15,16]. Due to their optical transparency in the visible range and tunable mechanics, hydrogels are a promising platform for delivering light to mobile peripheral nerves[17–21]. However, a number of technical challenges have precluded their effective implementation as optical nerve interfaces. The available hydrogel materials are susceptible to fatigue fracture from

recurring deformations during animal locomotion (Extended Data Figure 1c)[6,20,22]. The coupling of light into hydrogel fibers typically relies on rigid-soft interfaces between silica and hydrogels that are vulnerable to fatigue fracture during repeated mechanical loading[23]. Furthermore, the low refractive indices of fully hydrated hydrogels (~1.34) and poor refractive index contrast between the core and cladding materials lead to severe light leakage along the hydrogel fibers[20].

Here, we present fatigue-resistant hydrogel optical fibers that adapt to persistent locomotion in naturally behaving mice (Figure 1c). Polymeric nanocrystalline domains were introduced within the hydrogel fibers, which prevented crack propagation and ensured fiber resilience against repeated stretching (Figure 1d). Nanocrystalline domains were also generated at the silica-hydrogel interface to establish a robust light coupling with an external light source through a commercial silica fiber segment (Figure 1d). Additionally, the hydrogel fibers were equipped with a cuff at their distal end to facilitate robust contact with peripheral nerves during deformation (Figure 1e and Extended Data Figure 1d). In chronic voluntary wheel running assays, the hydrogel fibers successfully delivered blue light to the sciatic nerves, allowing optogenetic stimulation of hindlimb muscles in Thy1::ChR2-EYFP mice, which broadly express blue-light-sensitive cation channels channelrhodopsin 2 (ChR2) fused to an enhanced yellow fluorescent protein (EYFP) in their nervous systems. This technology was also applied to TRPV1::NpHR-EYFP mice, which express the yellow light-gated chloride pump halorhodopsin (NpHR) fused to EYFP in primary sensory afferents. In an inflammatory pain model, optical pulses delivered through the implanted hydrogel fibers to sciatic nerves yielded NpHR-mediated inhibition of pain hypersensitivity over an 8-week study.

Results

Fabrication of fatigue-resistant hydrogel optical fibers

To facilitate light delivery to the peripheral nervous system, we designed a hydrogel-based device that consists of a short silica segment to prevent hydrogel dehydration in air, a polyvinyl alcohol (PVA) hydrogel fiber with a core-cladding structure, and a hydrogel cuff attached to the targeted nerve (Figure 1c). An amorphous PVA hydrogel core was first chemically cross-linked within a tubular mold and directly connected to a short silica segment. Next, we converted the amorphous polymers to nanocrystalline domains at the silica-hydrogel interface and in the bulk hydrogel through annealing (Figure 1d and Extended Data Figure 2a,b). The presence of PVA nanocrystalline domains not only improved the hydrogel core's refractive index but also ensured a durable silica-hydrogel connection to minimize light loss. After annealing and rehydration, the hydrogel core was 600 μm in diameter and 6 cm in length. To prevent light leakage from the hydrogel core and thus avoid off-target illumination, we fabricated a hydrogel cladding (thickness: 200 μm) by dispersing and fixing light-absorbing nanomaterials, reduced graphene oxide (rGO, 0.21 wt%), within an amorphous PVA hydrogel[24]. During cladding synthesis, the PVA polymer chains interpenetrated and formed hydrogen bonds at the hydrogel core-cladding interface to ensure strong adhesion (Figure 1e and Extended Data Figure 2c). To create robust and

flexible contact with the targeted nerve, a hydrogel cuff was fabricated at the fiber distal end (Figure 1e).

Optical characterization of undeformed hydrogel fibers

For effective light delivery with minimal light loss, we first engineered the light absorption and scattering in the PVA hydrogel core by controlling the growth of nanocrystalline domains. Wide-angle X-ray scattering analysis revealed that 30-minute annealing generates nanocrystalline domains with an average size (d_{nd}) of 3.9 nm, which is two orders of magnitude smaller than the selected light wavelengths (λ = 473 nm for ChR2 activation and 589 nm for NpHR activation) (Figure 1f and Extended Data Figure 3a–c)[6,25]. The resultant PVA hydrogel material exhibited low light absorbance (Figure 1g). Extended annealing time and reduced chemical crosslinking generated more nanocrystalline domains, leading to structural heterogeneity in hydrogels and increased light absorbance (Extended Data Figure 3b–i).

Refractive index contrast between the hydrogel core (n_{core}) and cladding ($n_{cladding}$) can efficiently confine the light transmission within the hydrogel core. Therefore, we optimized their refractive indices by choosing the nanocrystalline PVA as the hydrogel core (n_{core} = 1.380), and amorphous PVA as the hydrogel cladding ($n_{cladding}$ = 1.342) (Figure 1h,i). Compared to amorphous hydrogels, nanocrystalline hydrogels exhibit a higher refractive index due to the lower water content and more densely packed nanocrystalline domains[20,26]. Ray tracing simulations confirmed that the increased contrast of refractive indices reduces light leakage (Extended Data Figure 3j,k). The light intensity collected from amorphous PVA hydrogel fibers is only 17% of that collected from nanocrystalline PVA hydrogel fibers of the same length (Extended Data Figure 3l,m). To further reduce light leakage, the hydrogel cladding was designed to be light-absorbing. A 200-μm-thick cladding made of amorphous rGO-PVA was generated with low light transmittances of 4.2% at 473 nm and 13.1% at 589 nm (Extended Data Figure 3n–q).

The resulting hydrogel fibers exhibited light attenuation coefficients of 1.07 dB cm^{-1} at 473 nm and 0.53 dB cm^{-1} at 589 nm at the fully hydrated state (Figure 1j,k). The optical performance maintained stable even when incubated in the physiological conditions for 6 months (1.09 ± 0.22 dB cm^{-1} at 473 nm, Extended Data Figure 3r). These attenuation coefficients are comparable to those seen in polymer fibers with GPa moduli[14,15]. When coupled to a light source (input: 45 mW) (Figure 1l), light delivered through a 6-cm-long hydrogel fiber is sufficient to trigger ChR2-mediated neuronal excitation (output: 35.4 mW mm^{-2})[27–29].

Optical characterization of deformed hydrogel fibers

We evaluated whether hydrogel fibers can maintain adequate light transmission during mechanical deformation. The hydrogel fibers possess a Young's modulus of 1.6 MPa, tensile strength of 3.0 MPa, and stretchability of 200% during a single-cycle tensile test (Figure 2a and Extended Data Figure 4a). This Young's modulus is 3–4 orders of magnitude lower than that of silica fibers (73 GPa) and previously reported polymer fibers (2.0 GPa for PC, 2.9 GPa for PMMA, and 2.6 GPa for COC)[14,30], improving mechanical matching with

biological tissues such as muscle (0.02 MPa) and sciatic nerve (0.6 MPa)[6,31]. To assess the fatigue resistance of the hydrogel fibers under physiological conditions, we subjected them to repeated mechanical loading in phosphate-buffered saline (PBS). The fatigue threshold of the silica-hydrogel interface was measured to be 625 J m^{-2}, comparable to the interfacial fatigue threshold found in the natural cartilage-bone interface (800 J m^{-2}) (Figure 2b and Extended Data Figure 4b). Commensurate with the loading frequency and mechanical strength of load-bearing muscles, we performed cyclic tensile tests on the hydrogel fibers with a frequency of 1 Hz and stress amplitude of 1.4 MPa[32,33]. These cyclic tests revealed that the maximum strain maintained ~70% over 10,000 cycles with no cavity or crack formation at the silica-hydrogel interface (Figure 2c,d). In addition, the hydrogel fibers exhibited resilience (0% hysteresis) and low modulus (1.6 MPa) even after cyclic loading (Extended Data Figure 4c). By performing cyclic stretching with different stress amplitudes, we determined the 30,000-cycle fatigue strength to be 1.4 MPa, similar to the strength of skeletal muscles (0.4–2.0 MPa) (Extended Data Figure 4d–f)[34]. Notably, no changes in mechanical behaviors were observed following their 8-week implantation in mice or 6-month incubation in PBS (Figure 2e,f and Extended Data Figure 4g,h).

We further investigated the optical transmission of the hydrogel fibers under cyclic stretching at a frequency of 1 Hz and a strain amplitude of 25%, which mimicked the mechanical loading occurring during locomotion (Figure 2g)[35]. We found that the hydrogel fibers maintained light transmission above 87% for more than 1,000 stretch cycles (Figure 2g,h and Supplementary Video 1). We subsequently evaluated the light transmission under extreme tensile loading. The hydrogel fiber transmitted 23% of maximum light intensity, even when elongated at a strain of 90%. Unlike stretchable hydrogel fibers, the silica fiber fractured at a strain of 1% and the polydimethylsiloxane (PDMS) fiber failed at a strain of 20% due to their low fracture energies (Figure 2i)[36,37]. We also measured the light transmission of different optical fibers under bending (Extended Data Figure 4i). Compared with common fiber materials, the hydrogel fibers showed high mechanical compliance and relatively low optical losses (Figure 2j)[38].

We also tested their adaptability to physiological tissue motion by attaching the fibers to a porcine artery ex vivo and simulating tissue deformation. Unlike silica fibers that constrained artery displacement, the hydrogel fibers followed tissue deformation and maintained stable light transmission under dynamic loading (Figure 2j,k and Supplementary Video 2). To expand their versatility, we designed fiber distal ends with different architectures, including a hydrogel cuff interfacing with tubular organs (e.g., peripheral nerves, Extended Data Figure 4j) and a conformal hydrogel membrane tailored to organs with smaller curvatures (e.g., heart, Extended Data Figure 4k).

Optogenetic stimulation after repeated fiber deformation

To demonstrate in vivo light delivery with repeated deformation, we implanted the hydrogel fibers in mice with voluntary wheel running tests (VWRTs), a standard locomotor activity test (Figure 3a). Transgenic Thy1::ChR2-EYFP mice, expressing excitatory opsins ChR2 in the nervous system (Figure 3b), were implanted with fibers and then subjected to periodic VWRTs (n = 6 mice, Figure 3c)[7,27]. During implantation, the hydrogel fiber's ferrule was

affixed on the skull while the cuff was wrapped around the sciatic nerve (Figure 3d). After implantation, the mice underwent 42-minute weekly VWRTs during which the repeated stance and swing phases were accompanied by fiber cyclic stretching. To quantify the deformation of the implanted fibers, mouse running gait during VWRTs was analyzed with DeepLabCut markerless pose estimation (Figure 3e,f and Supplementary Videos 3, 4)[39]. By tracking the fiber length in pose estimation during running, we found that the fiber stretching frequency and the strain amplitude were approximately 4 Hz and 10%, respectively, indicating that the implanted hydrogel fibers experienced ~10,000 stretches per week with the strain amplitude of ~10% (Figure 3e and Extended Data Figure 5a–c). The fiber deformation amplitudes during grooming and rearing were found to be comparable to or below those associated with running (Extended Data Figure 5d,e).

We then examined if light delivered through the hydrogel fibers could activate the motor axons in Thy1::ChR2-EYFP mouse sciatic nerves. After VWRTs, we recorded the electromyographic (EMG) signals in mouse hindlimb muscles under anesthesia in response to the pulsed blue light (wavelength: 473 nm, estimated light intensity: 35.4 mW mm^{-2}, frequency: 1 Hz, ON: 10 ms, OFF: 990 ms). Optical stimuli consistently induced EMG signals in the tibialis anterior (TA) or gastrocnemius (GN) muscles (Figure 3g and Extended Data Figure 6a–c). Besides, high-frequency optical pulses (40 Hz) resulted in tetanic muscle contractions (Extended Data Figure 6d). In the long run, optically evoked EMG potentials were recorded even 6 weeks after implantation (> 60,000 fiber stretching cycles), indicating stable mechanical and optical properties of hydrogel fibers in vivo (Figure 3h,i).

Effects of hydrogel fiber implantation on mice

To examine the potential effects of fiber implantation on locomotion, we first compared the running gait parameters during VWRTs, including stick diagrams, knee angles, ankle angles, and gait frequency, before and after the implantation surgery. With the exception of a minor decrease in the maximum ankle angle in the first 2 weeks following surgery, we did not observe any considerable effects of fiber implantation on general locomotor performance (Figure 3f and Extended Data Figure 5f–o). The results from von Frey tests indicated the implantation procedure did not cause mechanical allodynia (Extended Data Figure 7a–c). The skilled locomotor scores for the mouse hind paw on the implanted side temporarily decreased in horizontal ladder tests; however, their scores gradually returned to baseline levels during the recovery (Extended Data Figure 7d–f). To examine the potential inflammation, we harvested sciatic nerves after 8-week VWRTs and evaluated histology and immunohistochemistry. Histological evaluation showed that the implanted hydrogel cuffs did not cause severe foreign body reactions in the sciatic nerve at 8 weeks after implantation (Extended Data Figure 7g,h). Using ionized calcium-binding adapter molecule 1 (Iba1), a marker for macrophages in the peripheral nervous system[40,41], we also observed no significant increase in Iba1 expression in the implanted sciatic nerves compared to non-implanted ones (Extended Data Figure 7i–k, $P = 0.235$).

Furthermore, we examined possible adverse effects arising from optical illumination. Due to thermal dissipation within tissue, the photothermal effect in the sciatic nerves was found to be sustaintially smaller than that in air. At a coupled power of 45 mW, the temperature

increase (ΔT) measured at the distal end of the hydrogel fiber was < 0.4 °C, even at a 100% optical duty cycle (Extended Data Figure 8a–f). Notably, due to the optimized refractive index contrast between the core and cladding and the light absorption in the cladding, the radial leakage and off-target illumination along the fiber were minimized, enabling targeted experiments in transgenic animals broadly expressing opsins across the central and peripheral nervous systems (Extended Data Figure 8g–j). Additionally, we did not observe nerve dislocation due to fiber implantation and deformation during locomotion (Extended Data Figure 8k–m), nor architectural change in the hydrogel cuff following 8-week implantation in mice (Extended Data Figure 8n).

Optogenetic inhibition of nociception in behaving mice

We then evaluated the ability of the hydrogel optical fibers to modulate somatosensory neural pathways in behaving mice. To achieve this, we first created transgenic TRPV1::NpHR-EYFP mice, that expressed inhibitory rhodopsin NpHR fused with EYFP under the peptidergic nociceptor-specific promoter, transient receptor potential vanilloid receptor subtype 1 (TRPV1) (Figure 4a)[29]. Confocal microscopy images confirmed NpHR-EYFP expression in the dorsal root ganglia (DRGs) and the sciatic nerves of TRPV1::NpHR-EYFP mice (Figure 4b). To assess the efficacy of optogenetic inhibition in somatosensory afferents, we implanted hydrogel fibers in these mice and subjected them to sensory tests for up to 8 weeks. Chronic inflammatory pain was induced by intraplantar injection of complete Freund's adjuvant (CFA) 1 week following implantation, and maintained through biweekly incomplete Freund's adjuvant (IFA) injections (Figure 4c). Consistent with prior reports of the CFA inflammatory model, the mice developed mechanical allodynia (Figure 4d)[42,43]. To evaluate the effects of optogenetic inhibition on thermal sensitivity, we placed the mice on a hot plate at 50 °C, and recorded the latency of their first-time hind paw flinch paired with yellow light delivery to the sciatic nerves (wavelength: 589 nm, estimated light intensity: 8.5 mW mm^{-2}, frequency: 20 Hz, ON: 25 ms, OFF: 25 ms, 30-s duration) (Figure 4e)[42,44]. At the same optical illumination conditions, the hind paw on the implanted side (ipsilateral, ipsi-) in NpHR-expressing mice exhibited significantly longer flinch latencies compared to the non-implanted side (contralateral, contra-, $^{**}P = 0.0080$) and the control group (TRPV1::Cre, $^{****}P < 0.0001$) implanted with identical fibers (Figure 4f). Such diminished nocifensive behaviors upon light delivery were observed during the entire 8-week period (Figure 4g and Extended Data Figure 9a–e). Additionally, we employed von Frey tests to examine the effects of optogenetic silencing of TRPV1-expressing afferents on punctate mechanical allodynia, where normally innocuous tactile stimuli evoke pain (Figure 4h)[42,44]. Consistent with the effects on thermal sensitivity, in TRPV1::NpHR-EYFP mice, yellow light delivery through hydrogel fibers consistently attenuated mechanical allodynia over 8 weeks (Figure 4i,j and Extended Data Figure 9f–j), suggesting the utility of these fibers for studies of nociception in freely behaving mice.

Discussion

The hydrogel fiber technology offers a light delivery method for dynamic in vivo conditions, while preserving natural animal behaviors. By controlling the growth of polymeric nanocrystalline domains, we engineered fatigue-resistant hydrogel fibers with optimized

mechanical and optical properties. This technology is compatible with fiber-coupled light sources and molecular optogenetic tools commonly found in neuroscience laboratories. Utilizing optogenetics in the peripheral nervous system, our method can be further leveraged to investigate motor control, somatosensation, and pain processing[2,3,44]. Beyond the application in sciatic nerves, the hydrogel fibers can be tailored for implantation in peripheral nerves, as well as on other motile organs, such as the heart, gut, and blood vessels[15,45,46]. We envision the capability and adaptability of our hydrogel fiber technology being expanded for bi-directional optogenetics stimulation and optical recording via the use of fluorescence indicators[13,47]. Such advances will facilitate future studies of peripheral neurophysiology in naturally behaving animals.

Methods

Fabrication of short PVA-coated silica fibers.

A short silica fiber (core diameter 400 μm, length 15 mm) was stripped from a multimode optical fiber (Thorlabs FT400UMT) and fixed to a ceramic optical ferrule (Thorlabs CFX440–10) using an epoxy adhesive (Loctite Eccobond F112). The silica fiber was extruded out at one end of the optical ferrule with the length of 3 mm, and both ends of the silica fiber in the optical ferrule were polished. The extruded silica fiber was treated with 50% sodium hydroxide solution overnight and plasma cleaning (Harrick Plasma) in an oxygen atmosphere for 5 min. A solution of 10 wt% PVA solution was prepared by dissolving 10 g of PVA (molecular weight 146,000 to 186,000, 99+% hydrolyzed; Sigma-Aldrich) in 90 mL of water at 90 °C with continuous stirring for 5 hours until clear. A layer of PVA was deposited on the extruded silica fiber surface by dip coating in the 10 wt% PVA solution. After dip coating, the optical ferrule with a short PVA-coated silica fiber was dried at room temperature for 1 hour, heated at 100 °C for 1 hour, and rehydrated in water.

Fabrication of hydrogel optical fibers.

A solution of 10 wt% PVA solution was prepared by dissolving 10 g of PVA (molecular weight 146,000 to 186,000, 99+% hydrolyzed; Sigma-Aldrich) in 90 mL of water at 90 °C with continuous stirring for 5 hours until clear. Next, two separate mixtures were prepared by mixing 10 mL of 10 wt% PVA solution with 75 μL of hydrochloric acid (37% in water) for 30 seconds using a planetary centrifugal mixer (Thinky AR-100), and 10 mL of 10 wt% PVA solution with 75 μL of glutaraldehyde (GA) solution (25% in water) for 30 seconds, respectively. These two solutions were then mixed for 30 seconds and degassed for 2 minutes. The resultant mixture was infused into a silicone tubing mold (length 120 mm, diameter 1.6 mm; McMaster-Carr 5233K51) connected to a disk-shaped acrylic mold (diameter 3 mm, thickness 6 mm; acrylic sheet by laser cutting) at the distal end. A PVA-coated optical ferrule was then inserted into the proximal end of the silicone tubing mold. The mixture in the mold was allowed to cross-link for 6 hours at room temperature in a humid environment (relative humidity > 70%), after which the chemically cross-linked PVA hydrogel was demolded by swelling the silicone mold in dichloromethane (DCM; Sigma-Aldrich). A hole (diameter 0.91 mm) was punched through in the center of the disk-shaped PVA hydrogel at the distal end using a dispensing tip (20 Gauge; EFD Nordson). The PVA hydrogel fiber was next washed in excess water to remove residual chemicals for

3 days, dried in air at room temperature for 12 hours, annealed at 100 °C for 30 min, and rehydrated in water to generate the hydrogel fiber without cladding. The processes of drying and annealing usually induce substantial dimensional shrinkage of hydrogel fibers, during which the fibers were kept straight to prevent non-uniform deformation. After being fully hydrated in water, each hydrogel fiber without cladding was inserted into a silicone tubing (length 60 mm, diameter 1000 μm; McMaster-Carr 1972T14) with both ends exposed. A 5 mL of 10 wt% PVA solution was mixed with 50 μL of hydrochloric acid (37%) for 30 seconds using a planetary centrifugal mixer (Thinky AR-100). Another 5 mL of 10 wt% PVA solution was mixed with 50 μL of GA solution (25% in water) for 30 seconds. The above two solutions as well as a 5 mL of graphene oxide solution (6.2 g L^{-1} in water; Graphene Supermarket) were then mixed for 30 seconds and degassed for 2 minutes. The mixture was infused into the silicone tubing containing a hydrogel fiber without cladding, and left for chemical cross-linking for 12 hours, after which the hydrogel fiber with cladding was demolded by swelling the silicone mold in DCM. To reduce the graphene oxide in the hydrogel cladding, the hydrogel fiber was incubated in 100 mL of aqueous solution containing 5 g of sodium hydroxide and 1.5 g of sodium hydrosulfite at 37 °C for 1 minute to generate reduced graphene oxide. Lastly, the hydrogel fiber was washed with a large amount of water to remove residual chemicals for 2–3 days.

Attenuation measurement of hydrogel fibers.

The intensity of transmitted light through hydrogel fibers of various lengths were measured using a power meter (Thorlabs PM16–122) when the fibers were kept in a simulated tissue medium (1 wt% agarose gel). First, the hydrogel fiber was inserted into a plastic tube (diameter 3 mm). Then we injected 1 wt% agarose solution at 50 °C into the tube and allowed it to cool down. Next, a light source (maximum power 200 mW, wavelength 473 nm; Changchun New Industries) was coupled into a hydrogel fiber. We measured the light intensity at the fiber terminal after cutting a 5-mm-long segment repeatedly at an interval of 5 mm. The attenuation coefficients α of the hydrogel fibers were obtained by fitting the experimentally measured light intensity to the equation: $-10\log_{10}(P/P_0) = \alpha L + \text{const}$, where P is the light intensity at any fiber length L, P_0 is the light intensity when the fiber length is zero, and const is a constant value.

Light transmission measurement under deformation.

The light transmission through optical fibers made of silica, PDMS, and hydrogels were measured by a power meter (Thorlabs PM16–122), when the fibers were immersed in PBS. We used optic ferrules at both ends of the hydrogel fibers in the fabrication. We also connected both ends of PDMS fibers (Dow Corning Sylgard 184) with optic ferrules using glass-PDMS plasma bonding, and both ends of silica fibers (Thorlabs FT400UMT) with optic ferrules using epoxy adhesives (Loctite Eccobond F112). Then, one ferrule end of the fibers was coupled with a light source at 473 nm (maximum power 200 mW; Changchun New Industries), and another ferrule end was connected to a power meter to continuously measure the light intensity through optical fibers. During measurement, the fibers were immersed in PBS, and they were deformed using either a horizontal testing machine (CellScale) to stretch at different tensile strains or cylindrical discs to bend 360°

with different bending radii. The measurements of light transmission were conducted on 3–4 independent samples.

Mice.

All animal procedures followed animal care guidelines which had been reviewed and approved by the Committee on Animal Care at MIT and the Institutional Animal Care and Use Committee at UMass Amherst. Investigators were not blinded to the genotypes of the mice. Thy1::ChR2-EYFP (JAX 007612), TRPV1::Cre (JAX 017769), and RCL-eNpHR3.0/EYFP (Ai39, JAX 014539) mice were purchased from the Jackson Laboratory, and bred by the Division of Comparative Medicine at MIT and the Animal Care Service at UMass Amherst. The TRPV1::Cre mouse line expresses Cre recombinase under the control of the TRPV1 promoter, ensuring specific targeting of TRPV1-expressing cells. The RCL-eNpHR3.0/EYFP mouse line carries a Cre-dependent reporter construct with an enhanced halorhodopsin (eNpHR3.0). The breeding of TRPV1::NpHR-EYFP mice was carried out by crossing male homozygous TRPV1::Cre mice with female homozygous RCL-eNpHR3.0/EYFP mice. Genotyping of offspring was performed using polymerase chain reaction (PCR) analysis of ear snip DNA samples to confirm the presence of both TRPV1::Cre and RCL-eNpHR3.0/EYFP alleles. All mice were housed in plastic cages with disposable bedding on a standard light cycle (lights on at 7 am and off at 7 pm) with food and water available ad libitum. More detailed mouse information in Supplementary Table 1.

In vivo implantation of hydrogel optical fibers.

Mice were anesthetized with 1.5–2% isoflurane in oxygen, and their body temperature was maintained using a heated surgical table. Before surgical procedures, the skin areas on the hindlimb and head were cleaned with a depilatory agent (Nair Hair Remover Lotion) followed by povidone-iodine and ethanol scrub. Under sterile conditions, skin incisions were made on the head to expose the skull and on the hindlimb to expose the mid-thigh muscle. The vastus lateralis muscle and biceps femoris muscle were then bluntly separated to access the sciatic nerve. Next, a hydrogel fiber was threaded subcutaneously from the hindlimb incision to the head incision using a spatula. Next, the hydrogel cuff at the distal end of the hydrogel fiber was placed around the sciatic nerve. The cut on the hydrogel cuff was sealed with a tissue adhesive (B. Braun Histoacryl), and the skin incision on the hindlimb was then sutured back with Nylon 5–0 suture (Ethicon). Finally, the optical ferrule at the proximal end of the hydrogel fiber was affixed to the skull at a 10–20° angle to the horizontal with two self-curing dental cements (C&B Metabond Quick Cement System and Lang Jet Set-4). Thy1::ChR2-EYFP (n = 15), TRPV1::NpHR-EYFP (n = 13), and TRPV1::Cre (n = 7) mice were implanted with hydrogel fibers.

Voluntary wheel running tests.

Mice were placed on a wire mesh running wheel (diameter 20 cm; Prevue Pet Products) in an acrylic chamber to allow voluntary running before and after implantation. 1 day before surgery, the animals were habituated to the wheel for 42 minutes. Starting one week following fiber implantation, mice underwent 42-minute VWRTs weekly. Thy1::ChR2-EYFP mice (n = 6) with implanted hydrogel fibers were subjected to VWRTs during weeks 0–8 following surgery.

Gait analysis of mice behaviors.

We recorded the animal natural behaviors during running, grooming and rearing using a camera (Logitech Brio Ultra Pro HD Webcam). Then, we performed kinematic analysis on the recorded animal natural behaviors using a markerless pose estimation software (DeepLabcut)[39]. We labeled and tracked a few mouse body parts including ferrule, neck, back, iliac crest, hip, knee, ankle, and toes during animal behaviors. Using a custom algorithm written in MATLAB, a single gait cycle in VWRTs was determined between two local minimums in the plot of distance between the fore toe to hind toe over time, and divided into the swing phase and stance phase during VWRTs. The kinematic stick diagrams of hindlimb movement for a single gait cycle were extracted. The time-dependent fiber length was calculated from the total length of the segments between the ferrule and the middle point of the hip and knee. The initial fiber length was measured prior to the implantation surgery. From the time-lapse gait information, we obtained the variation of the knee angle, ankle angle, frequency of running gait and fiber stretching, and fiber strain.

Optogenetic stimulation in mice.

We performed the experiments of optogenetic muscle stimulation in Thy1::ChR2-EYFP mice during (week 0) and post (from week 1 to week 8) fiber implantation. Before the experiments, the mice just finished their weekly VWRTs. The experiments were performed when the mice were anesthetized with 1% isoflurane, and body temperature was maintained with a heated surgical table. For optical stimulus, a laser (wavelength 473 nm; Changchun New Industries) was connected to the optical ferrule on the mouse skull. Pulsed stimulation of 10-ms pulse width and 1 Hz frequency was applied (ON: 10 ms, OFF: 990 ms, 1% duty cycle) and delivered to the sciatic nerve through the implanted hydrogel fiber. By placing a power meter (Thorlabs PM16–122) at the distal end of the hydrogel fiber, we measured the in vitro light intensity to be 35.4 mW mm^{-1} and estimated the in vivo light intensity to be the same. For EMG recordings, an electrode was inserted into the ipsilateral GN muscle, and a reference electrode was subcutaneously inserted into the contralateral GN muscle. The pair of electrodes (Ultra Disposable Subdermal Needle Electrodes, Natus Medical) were attached to a PZ2–32 amplifier connected to RZ5D base processor (Tucker-Davis Technologies). We also changed stimulation parameters, including another frequency of optical pulses at 40 Hz, another light intensity at 145 mW mm^{-1}, and another position of the detection electrode in TA muscle. Thy1::ChR2-EYFP mice (n = 6) with implanted hydrogel fibers were subjected to optogenetic stimulation during weeks 0–8 following surgery.

Induction and maintenance of inflammatory pain.

Before evaluation of mechanical and thermal sensitivity in TRPV1::NpHR-EYFP and TRPV1::Cre mice, inflammatory pain was induced through intraplantar injection of complete Freund's adjuvant (CFA; Sigma-Aldrich F5881) or incomplete Freund's adjuvant (IFA; Sigma-Aldrich F5506) injection. CFA or IFA suspension was first diluted with an equal volume of 0.9% sodium chloride solution. Then, 10 μL of diluted CFA or IFA suspension was injected subcutaneously into the hind paw to generate localized inflammatory pain. TRPV1::NpHR-EYFP (n = 13) and TRPV1::Cre (n = 7) mice with implanted hydrogel fibers were subjected to CFA and IFA injections.

Evaluation of mechanical sensitivity using von Frey tests.

Mice were individually placed into a transparent acrylic chamber (length 7 cm, height 10 cm) with a metal mesh floor elevated 30 cm above a table. After a 30-minute habituation period, a series of eight calibrated von Frey monofilaments (bending force 0.04 g, 0.07 g, 0.16 g, 0.4 g, 0.6 g, 1 g, 1.4 g, 2 g; Bioseb) were applied to the plantar surface of the ipsilateral (implanted) or contralateral (non-implanted) hind paw for approximately 1 second, with a 30-second interval between each stimulus. Each monofilament was applied ten times, and the number of immediate hind paw flinch to each force was recorded. The force at which the paw flinch occurred at least six times was considered as the nociceptive threshold. Thy1::ChR2-EYFP (n = 9) mice with implanted hydrogel fibers were subjected to von Frey tests during weeks 0–4 following surgery, and TRPV1::NpHR-EYFP (n = 13) and TRPV1::Cre (n = 7) mice with implanted hydrogel fibers were subjected to von Frey tests during weeks 0–8 following surgery. All von Frey tests were performed in naturally moving mice.

Evaluation of thermal sensitivity using hot plate tests.

Mice were individually placed into a transparent acrylic chamber (diameter 19 cm, height 26 cm) on a heated metal surface (length 26.5 cm, width 26.5 cm) which was maintained at 50 ± 0.1 °C (Harvard Apparatus). Each hot plate test lasted for ≤ 30 seconds, with a 30-minute interval between each stimulus to prevent heat-related injury. The latency for a mouse to exhibit its first-time hind paw flinch was recorded, after which it was immediately removed from the hot plate. TRPV1::NpHR-EYFP (n = 13) and TRPV1::Cre (n = 7) mice with implanted hydrogel fibers were subjected to hot plate tests during weeks 0–8 following surgery. All hot plate tests were performed in naturally moving mice.

Optogenetic inhibition of nociception in naturally behaving mice.

We performed the experiments of optogenetic nociception inhibition in TRPV1::NpHR-EYFP and TRPV1::Cre mice from week 3 to week 8 post fiber implantation. During the experiments, the naturally behaving mice were subjected to von Frey and hot plate tests. For optical stimulus, a laser (maximum power 300 mW, wavelength 589 nm; Ningbo Yuanming Laser Technology) was connected to the optical ferrule on the mouse skull. Pulsed stimulation of 25-ms pulse width and 20 Hz frequency was applied (ON: 25 ms, OFF: 25 ms, 50% duty cycle) and delivered to the sciatic nerve through the implanted hydrogel fiber. By placing a power meter (Thorlabs PM16–122) at the distal end of the hydrogel fiber, we measured the in vitro light intensity to be 8.5 mW mm^{-1} and estimated the in vivo light intensity to be the same. For animal behavior tests, they underwent thermal and mechanical sensitivity tests, during which the yellow light pulses were delivered. TRPV1::NpHR-EYFP mice (week 3, n = 13; week 4, n = 12; week 5, n = 11; week 6–8, n = 10) in the test group and TRPV1::Cre mice (week 3–5, n = 7; week 6–8, n = 6) in the control group were subjected to optogenetic inhibition during weeks 0–8 following surgery.

Tissue harvesting.

Once mice were euthanized, their sciatic nerves and DRGs were removed from the body, washed briefly in PBS, and fixed in 4% paraformaldehyde for more than 48 h at 4 °C in

dark. For immunohistochemistry staining, fixed tissues were then placed in 30% sucrose in PBS overnight at 4 °C in dark. Next, the tissues were embedded in Tissue-Tek OCT compound (Sakura Finetek 4583), and cut into 20-μm transverse sections using a cryostat microtome (Leica CM1950).

Immunohistochemistry staining to confirm transgenic expression.

We performed immunohistochemistry staining for the transverse sections of TRPV1::NpHR-EYFP sciatic nerves to confirm the successful genetic crossing. A blocking solution containing 1 wt% bovine serum albumin (Sigma-Aldrich A9647) and 0.5 v/v% Triton X-100 (Sigma-Aldrich X100) was used for antibody dilution, and firstly added to the sciatic nerve slices for 30 min. The chicken pAb anti-GFP antibody (Abcam ab13970) as the primary antibody was diluted in the blocking solution at a ratio of 1:400, and incubated with the sciatic nerves overnight at 4℃. Then, the goat anti-chicken IgY (H+L), Alexa Fluor 488 (Invitrogen A-11039) as the secondary antibody was diluted in the blocking solution at a ratio of 1:1000, and incubated with the sciatic nerves for 2 h at room temperature. Meanwhile, the transverse sections of TRPV1::NpHR-EYFP DRGs and Thy1::ChR2-EYFP sciatic nerves did not require anti-GFP staining, and they were immersed in a blocking solution containing0.5 v/v% Triton X-100 for 30 min. Next, the anti-GFP stained and non-stained sections were placed on microscopic slides (Superfrost Plus Microscope Slide) and mounted with a mounting media containing 4′,6-diamidino-2-phenylindole (DAPI) (Fluoromount-G Mounting Medium with DAPI, Invitrogen). Finally, the slides were imaged under a confocal microscope (Leica TCS SP2) with a 40× oil immersion objective lens.

Statistical analysis.

Statistical analyses were performed in GraphPad Prism 9 and OriginPro 2023. We first performed Shapiro-Wilks tests for data normality. For independent data with normal distribution, we used one-way ANOVA with Tukey's multiple comparison test. For independent data with non-normal distribution, we used Kruskal-Wallis ANOVA with Dunn's multiple comparison test. For paired data with normal distribution, we used one-way repeated measures ANOVA with Tukey's multiple comparison test. For paired data with non-normal distribution, we used Friedman tests with Dunn's multiple comparison test. *P* values less than 0.05 were considered significant: *0.01 ≤ *P* < 0.05, **0.001 ≤ P < 0.01, **0.001 ≤ *P* < 0.01, ****P < 0.0001. The detailed statistical information for Figures, Extended Data Figures, and Supplementary Figures are indicated in the Supplementary Tables 2–21.

Extended Data

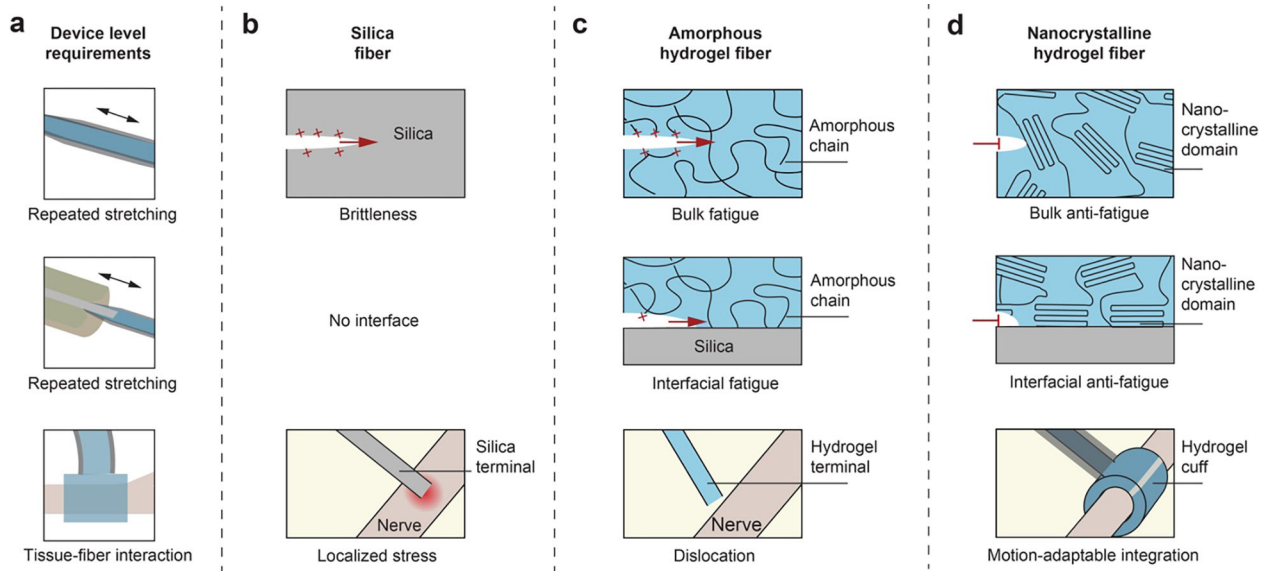

Extended Data Fig. 1. Mechanical design principles for peripheral nerve optogenetics.

a, Light delivery to peripheral nerves under persistent deformation faces challenges including repeated stretching of the bulk fiber and at the fiber-silica and the tissue-fiber interfaces. b, Using a silica fiber with high stiffness and high brittleness leads to fatigue failure under repeated stretching and localized mechanical stress at the silica fiber terminal. c, Using an amorphous hydrogel fiber with high compliance but high brittleness leads to fatigue failure under repeated stretching and no tissue integration at the hydrogel fiber terminal. d, Using a nanocrystalline hydrogel fiber with polymeric nanocrystalline domains leads to fatigue-resistance under repeated stretching and motion-adaptable integration between a hydrogel cuff and a target tissue.

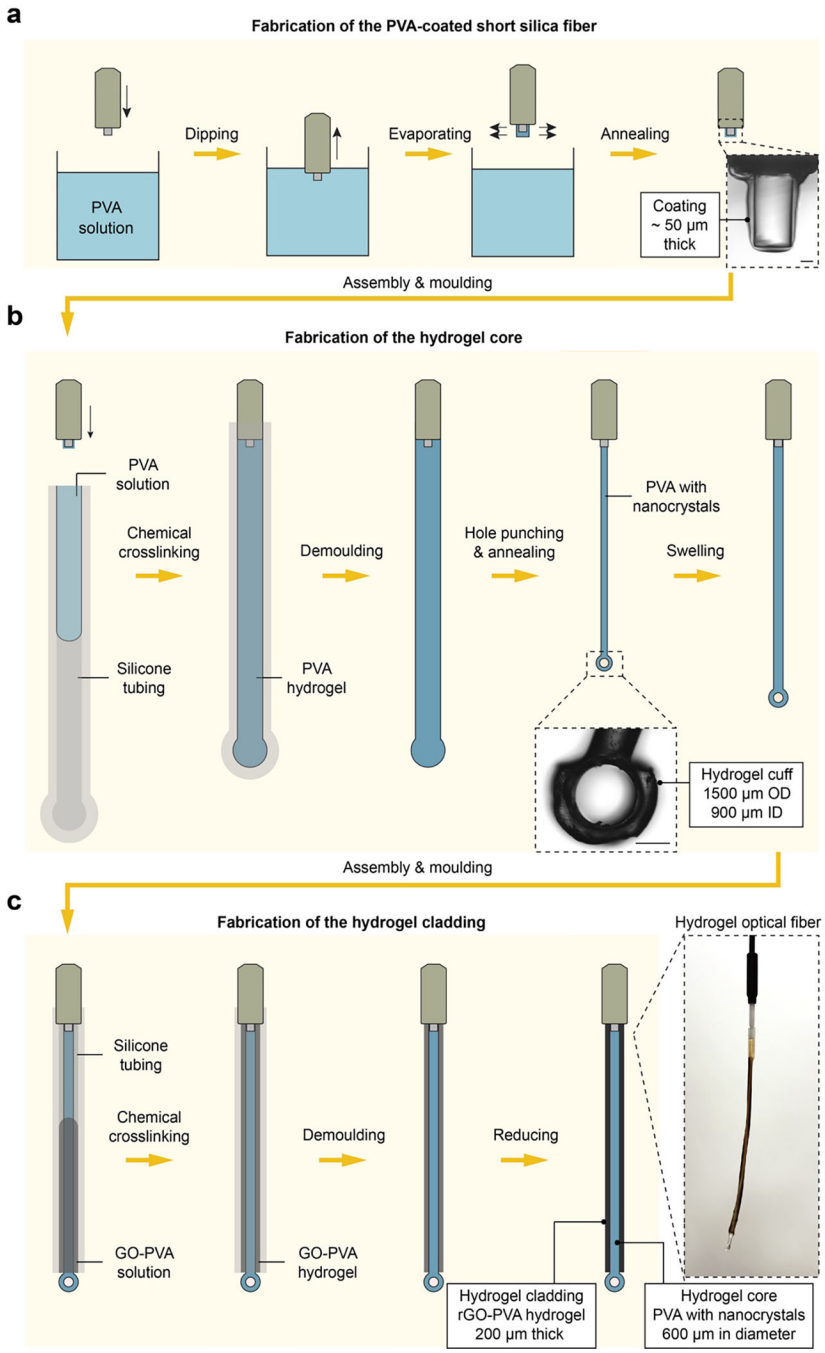

Extended Data Fig. 2. Fabrication procedures of hydrogel optical fibers.

a, Fabrication of polyvinyl alcohol (PVA)-coated short silica fibers. The silica fiber in a ceramic optic ferrule was dip-coated within a PVA solution, and then the PVA solution was allowed to dry and annealed to form the PVA hydrogel coating (50-μm-thick in the swollen state). b, Fabrication of hydrogel cores. The hydrogel core was fabricated by chemical crosslinking of the PVA solution in a silicone mold, together with the PVA-coated optic ferrule at one end and a disk-shaped compartment (3 mm in diameter) at the other end. The chemically crosslinked hydrogel core was then demoulded, washed, dried, annealed, and

swollen. By hole punching, the hydrogel cuff at the other end of the hydrogel core has the dimensions of 1500 μm in outer diameter and 900 μm in inner diameter in the dry state. c, Fabrication of hydrogel claddings. After inserting the hydrogel core into another silicone mold, the graphene oxide (GO)-PVA hydrogel was chemically crosslinked on the surface of the hydrogel core. After crosslinking and demoulding, it was then reduced to reduced graphene oxide (rGO)-PVA hydrogel cladding. The resulting hydrogel core is 600 μm in diameter and the hydrogel cladding is 200 μm thick. The inset is an image of a hydrogel fiber connected to a light source.

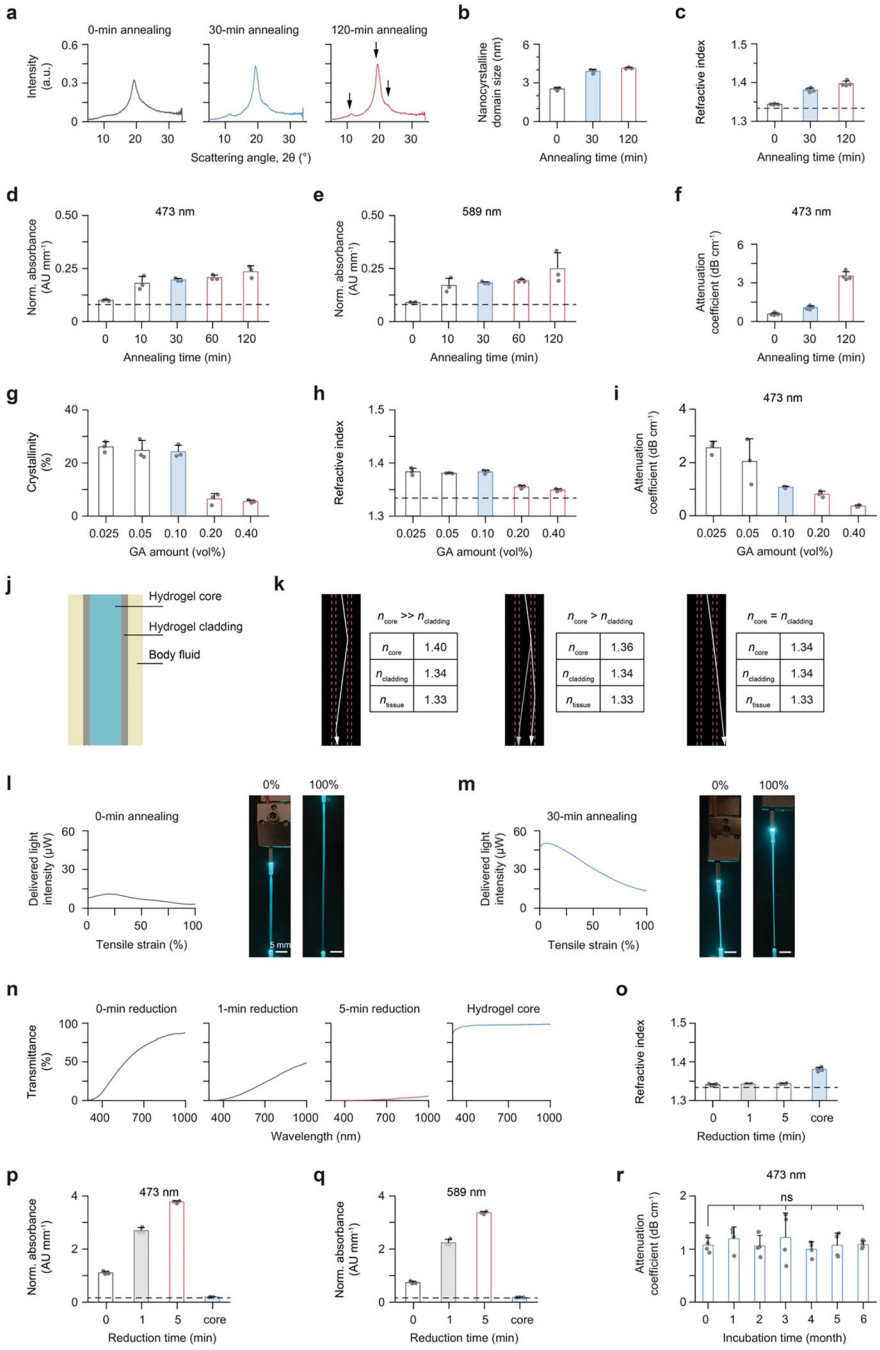

Extended Data Fig. 3. Engineered optical performances of hydrogel fibers.

a, Wide-angle X-ray scattering profiles for hydrogel core materials (dry state) with varied annealing times. b-e, Nanocrystalline domain size (b), refractive index (c), normalized absorbance at 473 nm (d), and normalized absorbance at 589 nm (e) for hydrogel core materials with varied annealing times. The dashed lines represent the values of PBS. AU: absorbance units. f, Attenuation coefficient at 473 nm for hydrogel fibers, in which the hydrogel core materials have varied annealing times. g-h, Crystallinity (g) and refractive index (h) for hydrogel core materials with varied glutaraldehyde (GA) amounts. The dashed

line represents the refractive index of PBS. i, Attenuation coefficient at 473 nm for hydrogel fibers, in which the hydrogel core materials have varied GA amounts. j-k, Schematic (j) and ray tracing simulation (k) of hydrogel fibers, in which the hydrogel core materials have varied refractive indices. l-m, Representative plots of light intensity delivered through hydrogel fibers in PBS vs. tensile strain, in which the hydrogel core materials have varied annealing time. The right images show the hydrogel fibers (no cladding) at different tensile strains with two ends connected to a light source and a photodetector, respectively. Scale bars: 5 mm. n, Transmittance spectra for hydrogel cladding materials with varied reduction times and the hydrogel core material. o-q, Refractive index (o), normalized absorbance at 473 nm (p), and normalized absorbance at 589 nm (q) for hydrogel cladding materials with varied reduction times and the hydrogel core material. The dashed lines represent the values of PBS. AU: absorbance units. r, Attenuation coefficient at 473 nm for hydrogel fibers over time when incubated in the PBS at 37 °C. ns: not significant.

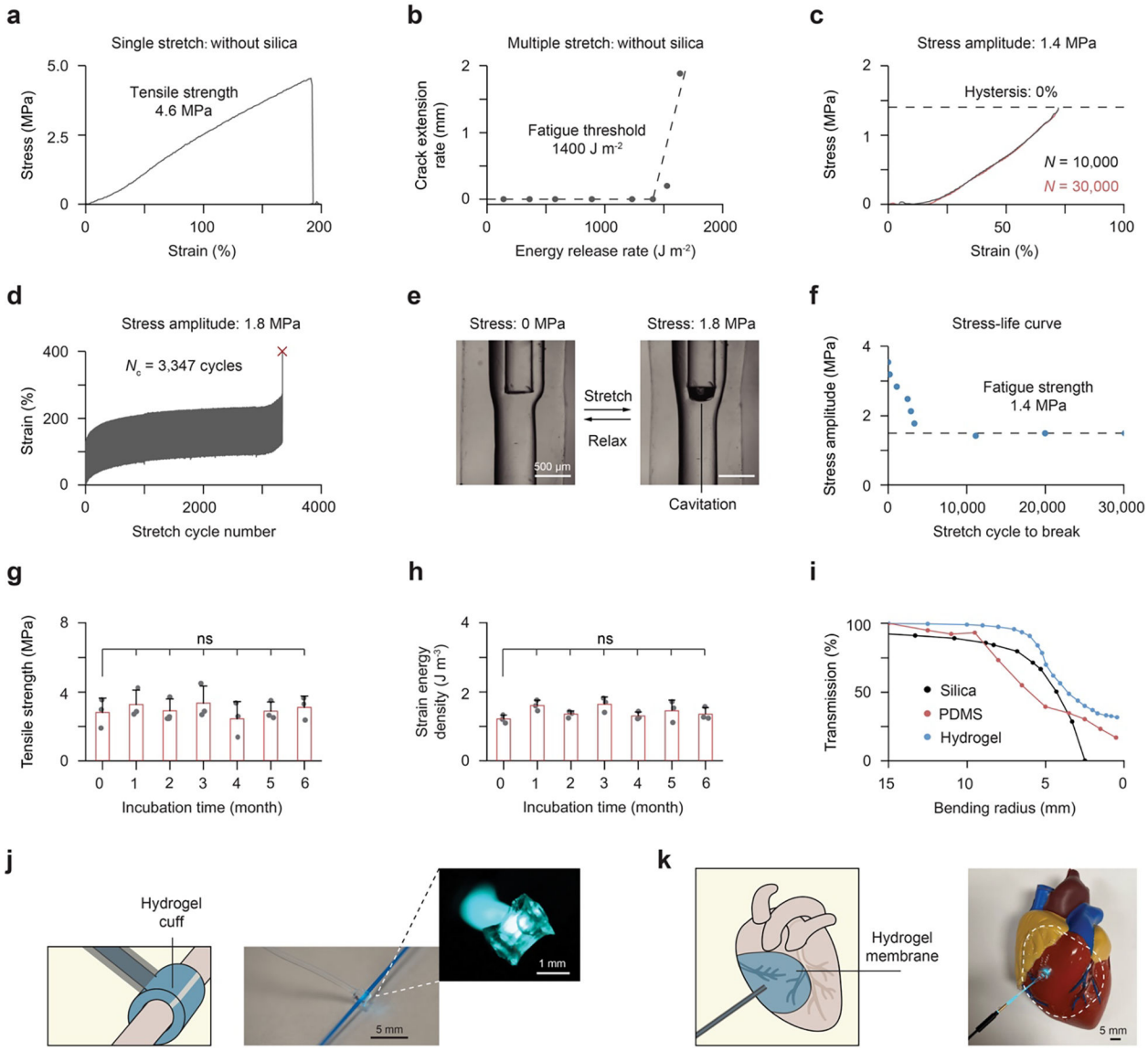

Extended Data Fig. 4. Engineered mechanical performances of hydrogel fibers.

a, Representative plot of nominal stress vs. strain of the hydrogel fiber (without silica) under single-cycle tensile test. The measured tensile strength is 4.6 MPa and Young's modulus is 1.8 MPa. b, Plot of crack extension rate vs. energy release rate of the hydrogel core material (without silica) under cyclic tensile test. The measured fatigue threshold is 1,400 J m-2. c, Plot of nominal stress vs. strain of the hydrogel fiber (with silica) under cyclic tensile test. The applied stress amplitude in the cyclic tensile test is 1.4 MPa and the cycle number is 10,000 and 30,000. The hysteresis for both stress-strain curves are 0%. d, Plot of strain vs. cycle number of the hydrogel fiber under cyclic tensile test. The applied stress amplitude in the cyclic tensile test is 1.8 MPa and the total cycle number (Nc) is 3,347. e, Microscopic images of the hydrogel fiber at different tensile stresses of 0 MPa and 1.8 MPa under cyclic tensile test. Cavitation happens at the hydrogel-silica interface when the applied stress amplitude is 1.8 MPa. Scale bars: 0.5 mm. f, Plot of applied stress amplitude vs. stretch cycle number to break of the hydrogel fiber (with silica), or the stress-life curve.

The measured fatigue strength is 1.4 MPa. g-h, Tensile strength (g) and strain energy density (h) for hydrogel fibers over time when incubated in the PBS at 37 °C. i, Representative plot of normalized light intensity vs. bending radius of the silica, PDMS, and hydrogel fibers in PBS. j-k, Schematic and image of a hydrogel cuff (j) and a hydrogel membrane (k) at the optical fiber terminal attached to artificial tissues (nerve and heart). The inset is an image of the hydrogel cuff in the dark field with light on. ns: not significant.

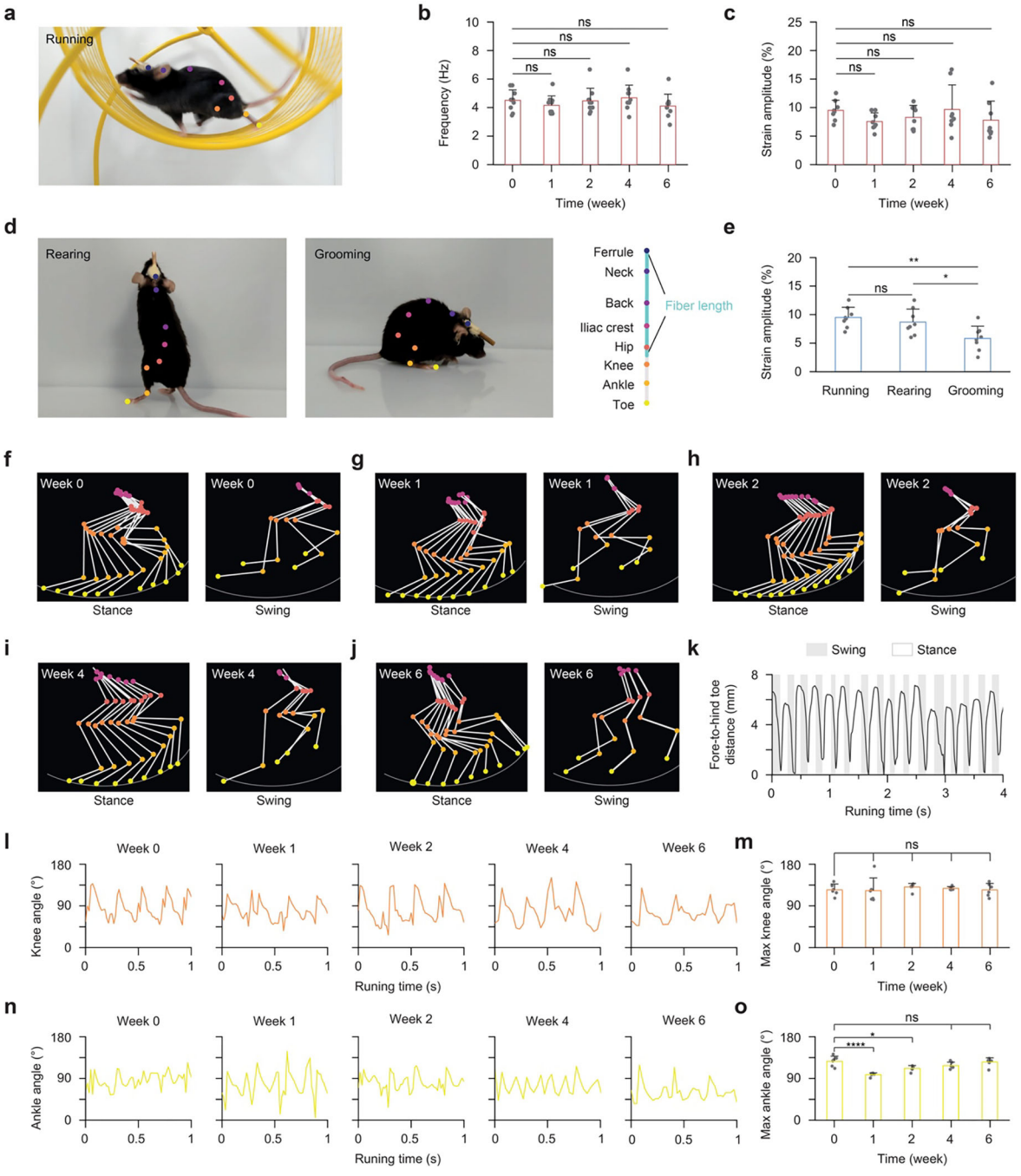

Extended Data Fig. 5. Gait analysis of mice implanted with hydrogel fibers.

a, Image of a mouse implanted with a hydrogel fiber moving on a running wheel. The mouse is labeled with nodes for the ferrule, neck, back, iliac crest, hip, knee, ankle, and toe. b-c, Frequency of gait cycle (i.e., fiber stretch cycle, b) and strain amplitude of hydrogel fibers (c) during mice movement on a running wheel from week 0 to week 6. d, Images of a mouse rearing and grooming when implanted with a hydrogel fiber. The mouse is labeled with nodes for the ferrule, neck, back, iliac crest, hip, knee, ankle, and toe. The fiber length, highlighted in blue, is calculated by the total length of the segments starting from the ferrule to the middle point between the hip and knee. e, Quantified strain amplitude of hydrogel fibers during mice running, rearing, and grooming. f-j, Kinematic stick diagram of mouse hindlimb movement on a running wheel on week 0 (f) before implantation, and week 1 (g), week 2 (h), week 4 (i) and week 6 (j) after implantation. A gait cycle is composed of a stance phase (left) and a swing phase (right) in the kinematic stick diagram. The nodes represent the iliac crest, hip, knee, ankle, and toe from top to bottom. k, Representative plot of distance between the fore toe to hind toe over time during mice movement on a running wheel. The total time period is divided into a few gait cycles, and each cycle is discomposed to a swing phase and a stance phase according to the positive or negative slope. l, Representative plots of knee angle variation during mice hindlimb movement on a running wheel from week 0 to week 6. m, Quantified maximum knee angle during mice hindlimb movement on a running wheel from week 0 to week 6. n, Representative plots of ankle angle variation during mice hindlimb movement on a running wheel from week 0 to week 6. o, Quantified maximum ankle angle during mice hindlimb movement on a running wheel from week 0 to week 6. ns: not significant.

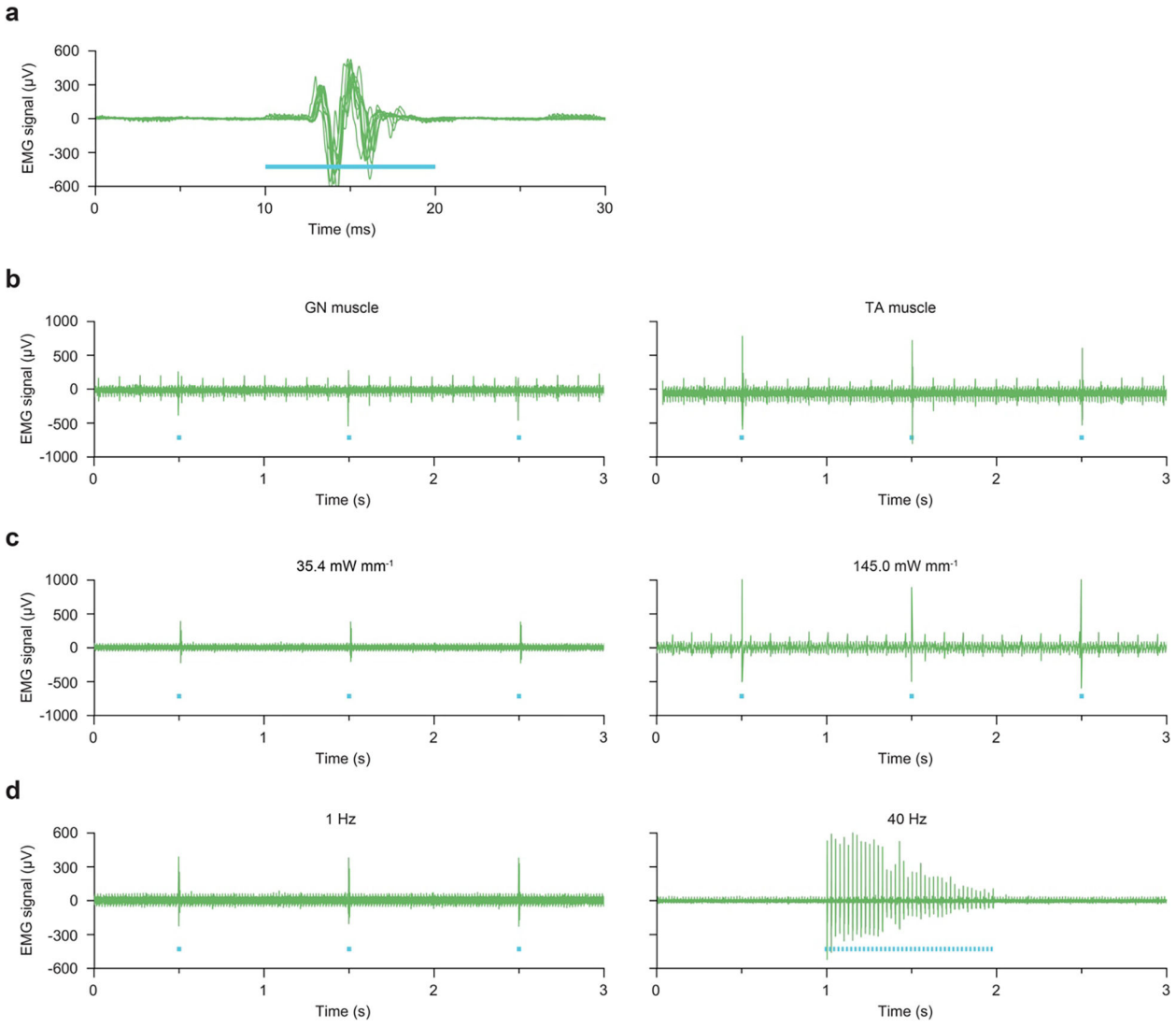

Extended Data Fig. 6. Optogenetic stimulation measured by EMG signals.

a, Overlay plot of EMG signals recorded on the GN muscle when the frequency of optical pulses is 1 Hz (ON: 10 ms, OFF: 990 ms) and the irradiance is 35.4 mW mm-2. b, Plots of EMG signals recorded on the GN muscle (left) and TA muscle (right) when the frequency of optical pulses is 1 Hz and the irradiance is 35.4 mW mm-2. c, Plots of EMG signals recorded on the GN muscle when the frequency of optical pulses is 1 Hz and the irradiance is 35.4 mW mm-2 (left) or 145.0 mW mm-2 (right). d, Plots of EMG signals recorded on the GN muscle when the frequency of optical pulses is 1 Hz (left) or 40 Hz (right), and the irradiance is 35.4 mW mm-2. Blue bars indicate optical pulses from a 473-nm light source.

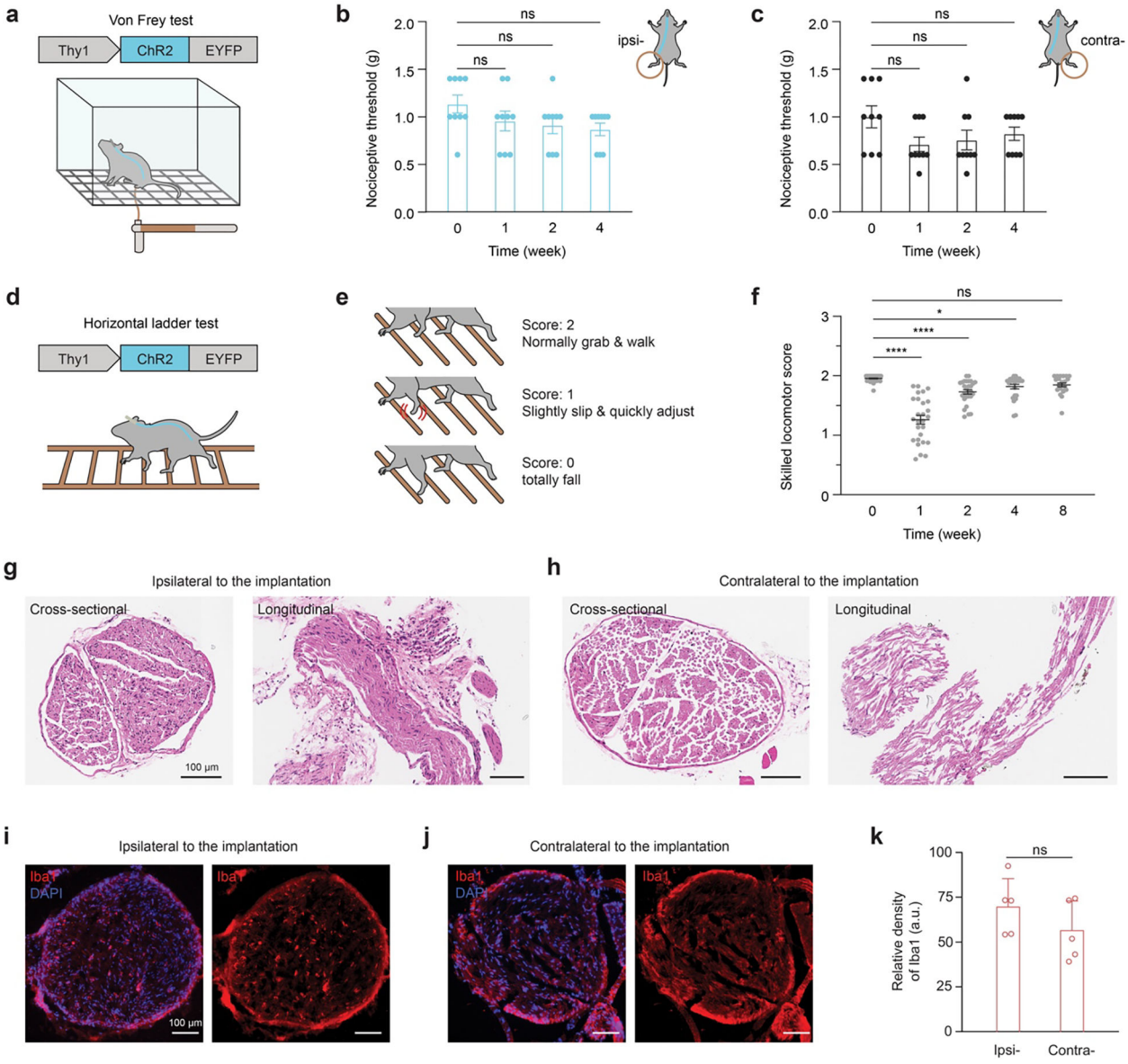

Extended Data Fig. 7. Behavior and biocompatibility tests of mice implanted with hydrogel fibers.

a, Schematic showing a Thy1::ChR2-EYFP mouse with a hydrogel fiber during von Frey tests. b-c, Nociceptive thresholds of ipsilateral (b) and contralateral (c) hind paw flinch in von Frey tests for Thy1::ChR2-EYFP mice over time after implantation. d, Schematic showing a Thy1::ChR2-EYFP mouse with a hydrogel fiber during horizontal ladder tests. e, Steps are counted and classified as either a normal walk (score 2), a slight slip (score 1), and a fall (score 0). f, Skilled locomotor score of ipsilateral hind paws for Thy1::ChR2-EYFP mice over time after implantation. g-h, Representative histological images of TRPV1::NpHR-EYFP mice's ipsilateral (g) and contralateral (h) sciatic nerves. Sciatic nerves were harvested 8 weeks after implantation, and stained using hematoxylin and eosin (H&E). Blue: cell nuclei by hematoxylin; pink: extracellular matrix and cytoplasm by eosin. Scale bars: 100 μm. i-j, Representative immunohistochemistry images of Thy1::ChR2-EYFP

mice's ipsilateral (i) and contralateral (j) sciatic nerves. Sciatic nerves were harvested 8 weeks after implantation, and stained using anti-Iba1 antibodies for macrophages. Red: Iba1; blue: DAPI. Scale bars: 100 μm. k, Iba1 relative densities in both ipsilateral and contralateral sciatic nerves. ns: not significant.

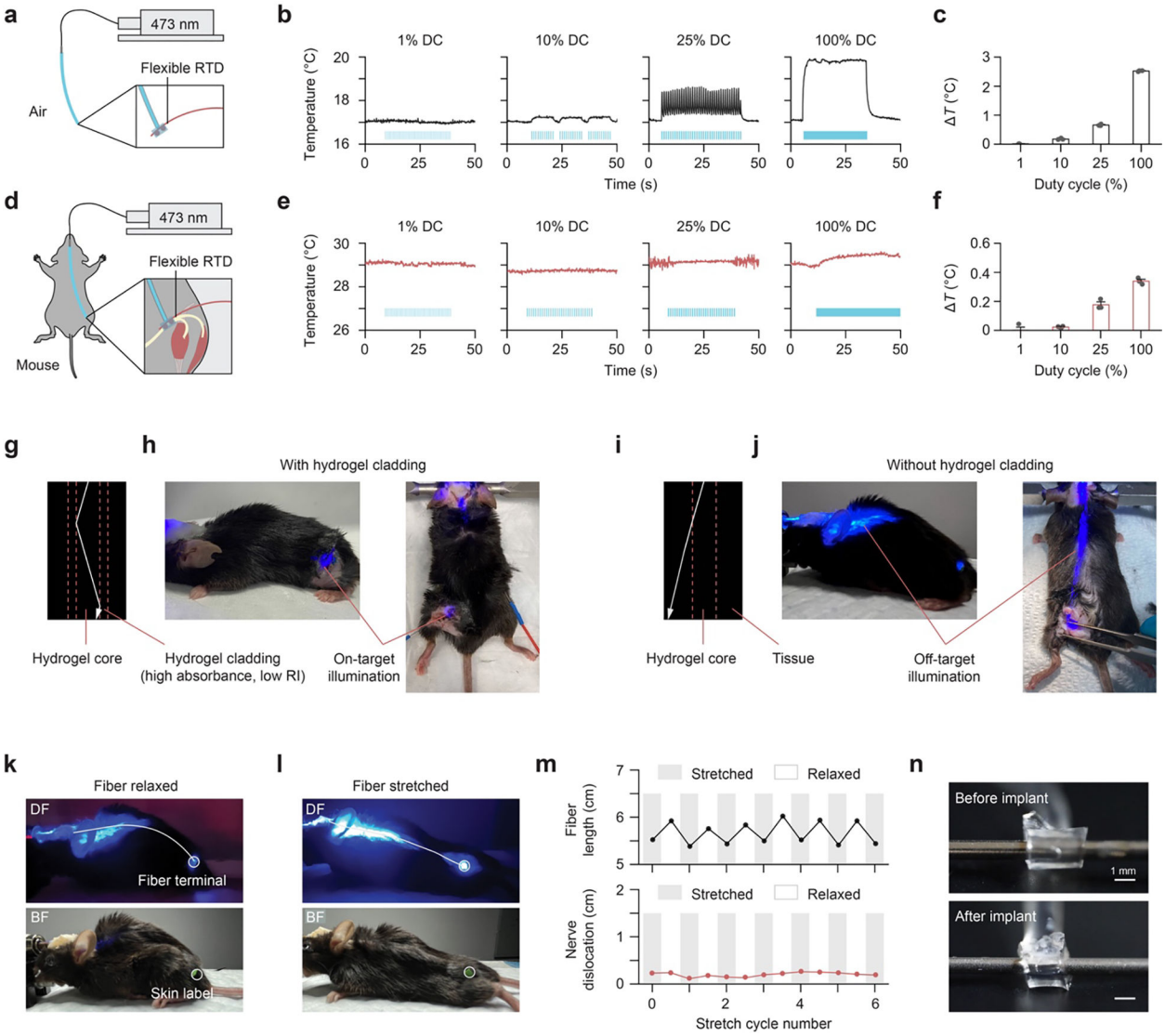

Extended Data Fig. 8. Evaluation of optical illumination through implanted hydrogel fibers.

a, Schematic of the temperature measurement through a resistance temperature detector (RTD) at the hydrogel cuff in air. The light source delivers 473-nm optical pulses with an irradiance of 35.4 mW mm-2. b, Plots of temperature variation in air when the optical pulses exhibit different duty cycles (DCs). Blue bars indicate optical pulses. c, Temperature increase in air under optical pulses with different DCs. d, Schematic of the temperature measurement through an RTD at the hydrogel cuff in mice. The light source delivers 473-nm optical pulses with an irradiance of 35.4 mW mm-2. e, Plots of temperature variation in mice when the optical pulses exhibit different DCs. Blue bars indicate optical pulses. f, Temperature increase in mice under optical pulses with different DCs. g, Ray

tracing simulation of hydrogel fibers with the hydrogel cladding. h, Images of a mouse implanted with a hydrogel fiber with the hydrogel cladding, showing on-target illumination. i, Ray tracing simulation of hydrogel fibers without the hydrogel cladding. j, Images of a mouse implanted with a hydrogel fiber without the hydrogel cladding, showing off-target illumination. k-l, Darkfield (DF) and brightfield (BF) images of a mouse implanted with a hydrogel fiber (no cladding) when the fiber is relaxed (k) and stretched (l). Contours of the hydrogel fiber without cladding are visible in the darkfield. The skin on top of the sciatic nerve is labeled with a green sticker to identify the original sciatic nerve position. m, Change of fiber length and nerve dislocation over fiber stretch cycles. n, Images of the hydrogel cuff before and after 8-week implantation in mice.

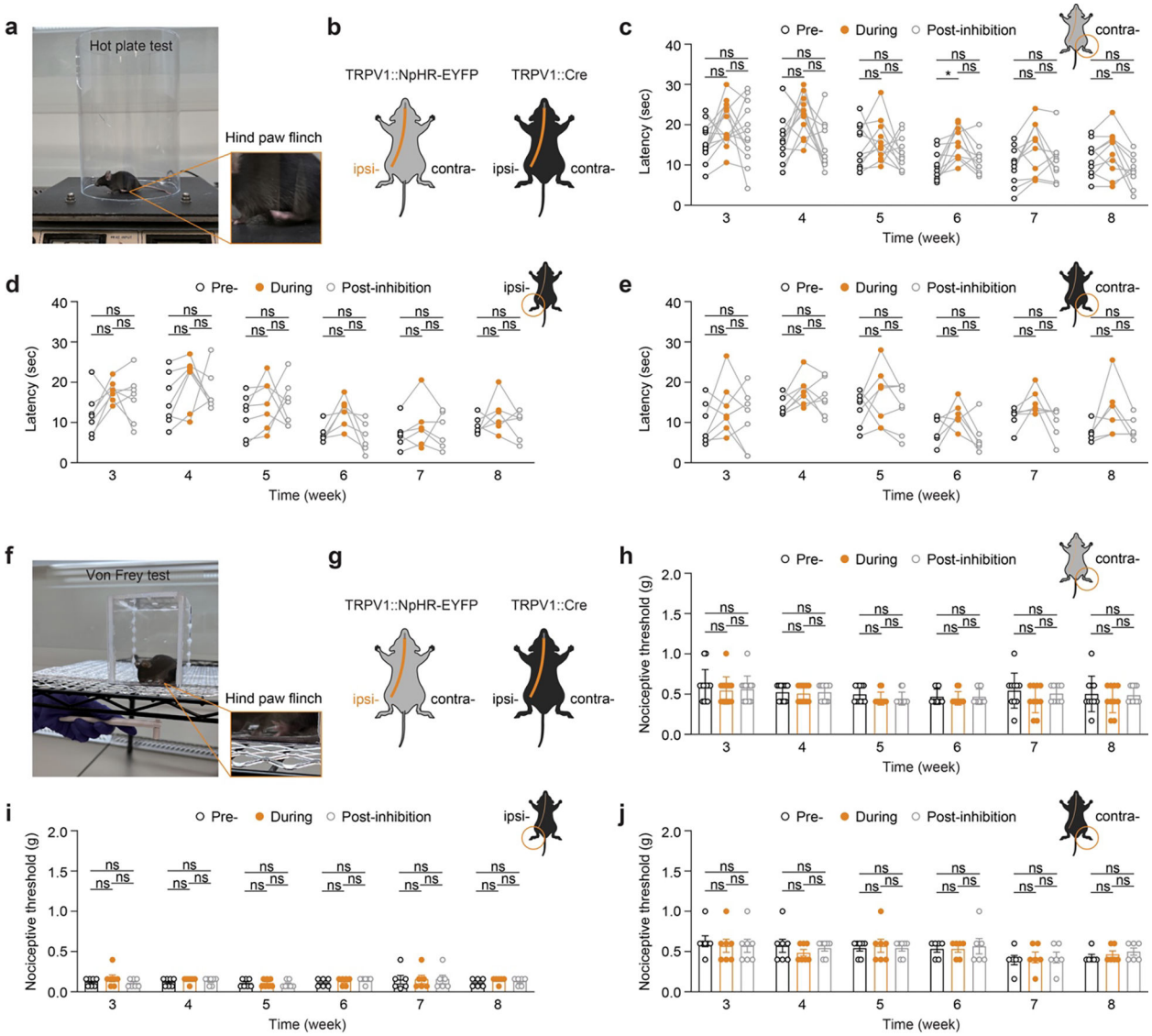

Extended Data Fig. 9. Optogenetic inhibition of nociception in naturally behaving mice enabled by hydrogel fibers (control and contralateral).

a, Image of the experimental setup for hot plate tests, during which animal hind paw flinches were observed. b, Schematic of TRPV1::NpHR-EYFP mice (test group) and TRPV1::Cre

mice (control group) with ipsilateral and contralateral hind paws. Yellow optical pulses were applied with a pulse width of 25 ms and irradiance of 8.5 mW mm-2. c, Latency of first-time contralateral hind paw flinch in hot plate tests for TRPV1::NpHR-EYFP mice over time after implantation. d, Latency of first-time ipsilateral hind paw flinch in thermal nociception tests for TRPV1::Cre mice over time after implantation. e, Latency of first-time contralateral hind paw flinch in thermal nociception tests for TRPV1::Cre mice over time after implantation. f, Image of the experimental setup for von Frey tests, during which animal hind paw flinch were observed. g, Schematic of TRPV1::NpHR-EYFP mice (test group) and TRPV1::Cre mice (control group) with ipsilateral and contralateral hind paws. Yellow optical pulses were applied with a pulse width of 25 ms and irradiance of 8.5 mW mm-2. h, Nociceptive threshold of contralateral hind paw flinch in von Frey tests for TRPV1::NpHR-EYFP mice over time after implantation. i, Nociceptive threshold of ipsilateral hind paw flinch in von Frey tests for TRPV1::Cre mice over time after implantation. j, Nociceptive threshold of contralateral hind paw flinch in von Frey tests for TRPV1::Cre mice over time after implantation. ns: not significant.

Supplementary Material

Refer to Web version on PubMed Central for supplementary material.

Acknowledgements

This work is supported in part by the National Institutes of Health (1R01HL153857–01, X.Z.), National Science Foundation (EFMA-1935291, X.Z.), the US Army Research Office through the Institute for Soldier Nanotechnologies at MIT (W911NF-13-D-0001, X.Z.), National Institutes of Health (1K99MH120279, 4R00MH120279, S.R.), Brain and Behavior Research Foundation (29878, S.R), UMass Amherst Faculty Research Grant (P1FRG0000000295, S.R.), National Institute of Neurological Disorders and Stroke (R01-NS086804 and R01-NS115025, P.A.), the McGovern Institute for Brain Research (P.A.), the Hock E. Tan and K. Lisa Yang Center for Autism Research (P.A.), and K. Lisa Yang Brain-Body Center (P.A.). A.S. was supported by the Lore Harp McGovern Fellowship.

Data Availability

The data associated with this study are available in the article and the Supplementary Information. The original data of material characterization, optogenetic stimulation, biocompatibility test, behavior test, and pain inhibition, as well as the codes for EMG data extraction, running cycle counting, and horizontal walk scoring, have been deposited in the public proteomics repository Figshare (https://figshare.com) and are accessible at https://doi.org/10.6084/m9.figshare.c.6703152.v2. Additional data beyond that provided in the figures and Supplementary Information are available from the corresponding author on request.

References

1. Deisseroth K Optogenetics. Nature Methods 8, 26–29 (2011). [PubMed: 21191368]
2. Kim CK, Adhikari A & Deisseroth K Integration of optogenetics with complementary methodologies in systems neuroscience. Nature Reviews Neuroscience 18, 222–235 (2017). [PubMed: 28303019]

3. Montgomery KL, Iyer SM, Christensen AJ, Deisseroth K & Delp SL Beyond the brain: Optogenetic control in the spinal cord and peripheral nervous system. Science Translational Medicine 8, 337rv335–337rv335 (2016).
4. Nam S & Mooney D Polymeric tissue adhesives. Chemical Reviews (2021).
5. Chen R, Canales A & Anikeeva P Neural recording and modulation technologies. Nature Reviews Materials 2, 1–16 (2017).
6. Liu X, Liu J, Lin S & Zhao X Hydrogel machines. Materials Today (2020).
7. Park SI et al. Soft, stretchable, fully implantable miniaturized optoelectronic systems for wireless optogenetics. Nature Biotechnology 33, 1280–1286 (2015).
8. Kathe C et al. Wireless closed-loop optogenetics across the entire dorsoventral spinal cord in mice. Nature Biotechnology (2021).
9. Michoud F et al. Epineural optogenetic activation of nociceptors initiates and amplifies inflammation. Nature Biotechnology 39, 179–185 (2021).
10. Zhang Y et al. Battery-free, fully implantable optofluidic cuff system for wireless optogenetic and pharmacological neuromodulation of peripheral nerves. Science Advances 5, eaaw5296 (2019). [PubMed: 31281895]
11. Brooks SP & Dunnett SB Tests to assess motor phenotype in mice: a user's guide. Nature Reviews Neuroscience 10, 519–529 (2009). [PubMed: 19513088]
12. Canales A et al. Multifunctional fibers for simultaneous optical, electrical and chemical interrogation of neural circuits in vivo. Nature Biotechnology 33, 277–284 (2015).
13. Park S et al. Adaptive and multifunctional hydrogel hybrid probes for long-term sensing and modulation of neural activity. Nature Communications 12, 3435 (2021).
14. Lu C et al. Flexible and stretchable nanowire-coated fibers for optoelectronic probing of spinal cord circuits. Science Advances 3, e1600955 (2017). [PubMed: 28435858]
15. Buchanan KL et al. The preference for sugar over sweetener depends on a gut sensor cell. Nature Neuroscience 25, 191–200 (2022). [PubMed: 35027761]
16. Sparta DR et al. Construction of implantable optical fibers for long-term optogenetic manipulation of neural circuits. Nature Protocols 7, 12–23 (2012).
17. Liu Y et al. Soft and elastic hydrogel-based microelectronics for localized low-voltage neuromodulation. Nature Biomedical Engineering 3, 58–68 (2019).
18. Tringides CM et al. Viscoelastic surface electrode arrays to interface with viscoelastic tissues. Nature Nanotechnology, 1–11 (2021).
19. Yuk H, Wu J & Zhao X Hydrogel interfaces for merging humans and machines. Nature Reviews Materials 7, 935–952 (2022).
20. Guo J et al. Highly stretchable, strain sensing hydrogel optical fibers. Advanced Materials 28, 10244–10249 (2016). [PubMed: 27714887]
21. Choi M et al. Light-guiding hydrogels for cell-based sensing and optogenetic synthesis in vivo. Nature Photonics 7, 987–994 (2013). [PubMed: 25346777]
22. Bai R, Yang J & Suo Z Fatigue of hydrogels. European Journal of Mechanics A 74, 337–370 (2019).
23. Liu J et al. Fatigue-resistant adhesion of hydrogels. Nature Communications 11, 1071 (2020).
24. Kashyap S, Pratihar SK & Behera SK Strong and ductile graphene oxide reinforced PVA nanocomposites. Journal of Alloys and Compounds 684, 254–260 (2016).
25. Oster G The scattering of light and its applications to chemistry. Chemical Reviews 43, 319–365 (1948). [PubMed: 18887959]
26. Rinawati M, Triastuti J & Pursetyo KT Characterization of elasticity and hydration of composite hydrogel based on collagen-iota carrageenan as a corneal tissue engineering. IOP Conference Series: Earth and Environmental Science 137, 012042 (2018).
27. Zheng H et al. A shape-memory and spiral light-emitting device for precise multisite stimulation of nerve bundles. Nature Communications 10, 2790 (2019).
28. Liske H, Qian X, Anikeeva P, Deisseroth K & Delp S Optical control of neuronal excitation and inhibition using a single opsin protein, ChR2. Scientific Reports 3, 3110 (2013). [PubMed: 24173561]

29. Iyer SM et al. Virally mediated optogenetic excitation and inhibition of pain in freely moving nontransgenic mice. Nature Biotechnology 32, 274–278 (2014).
30. Antunes P, Domingues F, Granada M & André P Mechanical properties of optical fibers. (INTECH Open Access Publisher, 2012).
31. Guimarães CF, Gasperini L, Marques AP & Reis RL The stiffness of living tissues and its implications for tissue engineering. Nature Reviews Materials 5, 351–370 (2020).
32. Kuthe CD, Uddanwadiker RV & Ramteke A Experimental evaluation of fiber orientation based material properties of skeletal muscle in tension. Molecular & cellular biomechanics : MCB 11, 113–128 (2014). [PubMed: 25831858]
33. Zwirner J, Ondruschka B, Scholze M & Hammer N Passive load-deformation properties of human temporal muscle. Journal of Biomechanics 106, 109829 (2020). [PubMed: 32517987]
34. Kuthe CD & Uddanwadiker RV Investigation of effect of fiber orientation on mechanical behavior of skeletal muscle. Journal of Applied Biomaterials Functional Materials 14, 154–162 (2016).
35. Layton B & Sastry A A mechanical model for collagen fibril load sharing in peripheral nerve of diabetic and nondiabetic rats. J. Biomech. Eng. 126, 803–814 (2004). [PubMed: 15796339]
36. Wang Z et al. Stretchable materials of high toughness and low hysteresis. Proceedings of the National Academy of Sciences 116, 5967–5972 (2019).
37. Griffith AA VI. The phenomena of rupture and flow in solids. Philosophical transactions of the royal society of london. Series A, containing papers of a mathematical or physical character 221, 163–198 (1921).
38. Park S, Loke G, Fink Y & Anikeeva P Flexible fiber-based optoelectronics for neural interfaces. Chemical Society Reviews 48, 1826–1852, doi:10.1039/C8CS00710A (2019). [PubMed: 30815657]
39. Nath T et al. Using DeepLabCut for 3D markerless pose estimation across species and behaviors. Nature Protocols 14, 2152–2176 (2019). [PubMed: 31227823]
40. Chiu IM et al. Activation of innate and humoral immunity in the peripheral nervous system of ALS transgenic mice. 106, 20960–20965, doi:doi:10.1073/pnas.0911405106 (2009).
41. Kalinski AL et al. Analysis of the immune response to sciatic nerve injury identifies efferocytosis as a key mechanism of nerve debridement. eLife 9, e60223, doi:10.7554/eLife.60223 (2020). [PubMed: 33263277]
42. Liu Y et al. Touch and tactile neuropathic pain sensitivity are set by corticospinal projections. Nature 561, 547–550 (2018). [PubMed: 30209395]
43. Boettger MK et al. Differences in inflammatory pain in nNOS-, iNOS- and eNOS-deficient mice. European Journal of Pain 11, 810–818 (2007). [PubMed: 17395508]
44. Basbaum AI, Bautista DM, Scherrer G & Julius D Cellular and Molecular Mechanisms of Pain. Cell 139, 267–284 (2009). [PubMed: 19837031]
45. Hsueh B et al. Cardiogenic control of affective behavioural state. Nature 615, 292–299 (2023). [PubMed: 36859543]
46. Sahasrabudhe A et al. Multifunctional microelectronic fibers enable wireless modulation of gut and brain neural circuits. Nature Biotechnology, doi:10.1038/s41587-023-01833-5 (2023).
47. Gunaydin LA et al. Natural neural projection dynamics underlying social behavior. Cell 157, 1535–1551 (2014). [PubMed: 24949967]

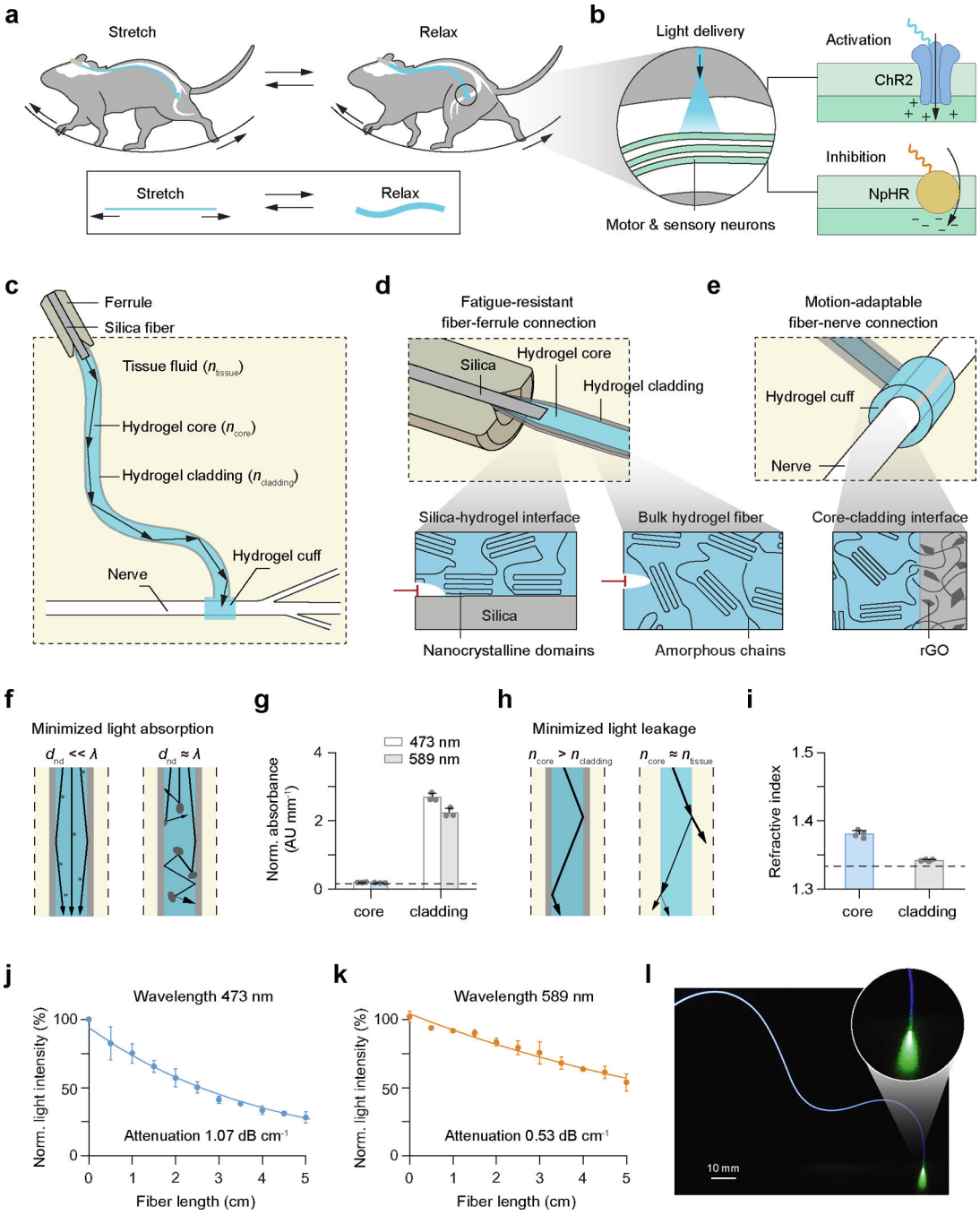

Figure 1. Design and mechanisms of hydrogel optical fibers.

a, Hydrogel fibers implanted under the skin can be used for light delivery to peripheral nerves. The implanted hydrogel fiber experiences repeated stretching during animal locomotion. **b,** Light delivered through the hydrogel fiber can be used for optogenetic activation or inhibition of motor and sensory neurons expressing opsins (e.g., ChR2 and NpHR) in peripheral nerves. **c,** Schematic of a hydrogel fiber composed of a short silica fiber in a ceramic optic ferrule, a hydrogel core, a hydrogel cladding, and a hydrogel cuff in the tissue fluid. **d,** Hydrogel core material adheres to a short silica fiber, enabling the

fatigue-resistant connection between the ferrule and fiber. The silica-hydrogel interface and hydrogel core material are fatigue-resistant as cracks are pinned by nanocrystalline domains. **e,** Hydrogel cuff wraps around a targeted nerve, enabling the motion-adaptable connection between the nerve and fiber. The hydrogel core-cladding interface is achieved by polymer chain interpenetration. **f,** Hydrogel core material contains nanocrystalline domains (d_{nd}) that are much smaller than the light wavelength (λ), enabling minimized light absorption and scattering. **g,** Normalized absorbance at 473 nm and 589 nm for the hydrogel core and hydrogel cladding materials. The dashed line represents the absorbance of PBS. AU: absorbance units. **h,** Hydrogel core material exhibits a higher refractive index than that of the hydrogel cladding material and tissue fluid, enabling minimized light leakage at the core-cladding interface. **i,** Refractive index for the hydrogel core and cladding materials. The dashed line represents the refractive index of PBS. **j-k**, Plot of normalized light intensity vs. fiber length at 473 nm (**j**) and 589 nm (**k**). The measured attenuation coefficients are 1.07 dB cm^{-1} at 473 nm and 0.53 dB cm^{-1} at 589 nm. **l,** Representative image of blue light delivery through a deformed hydrogel fiber (no cladding and cuff). The inset is the zoomed-in image of the fiber distal end directed to a calcein AM solution. Scale bar: 10 mm.

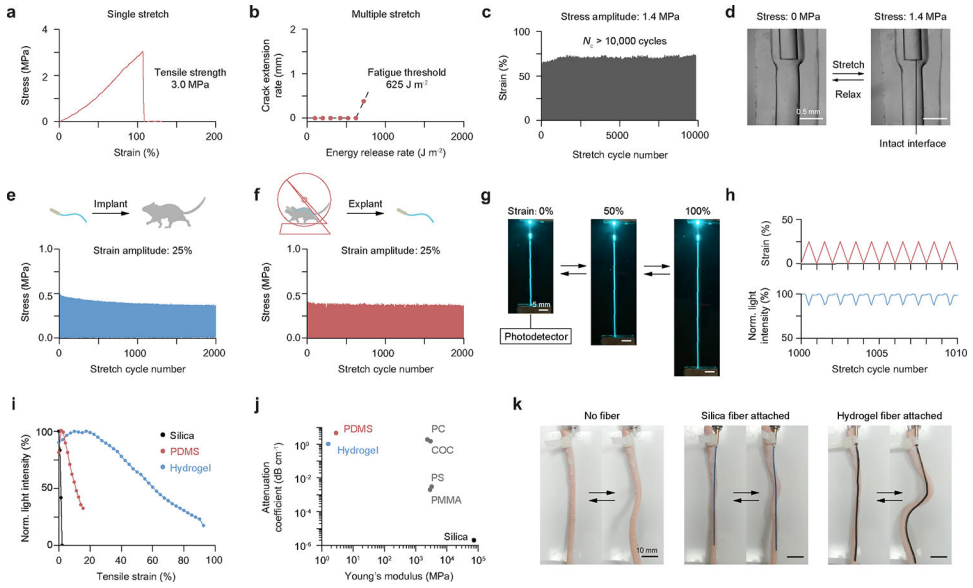

Figure 2. Mechanical robustness and flexibility of hydrogel optical fibers.

a, Representative plot of nominal stress vs. strain of the hydrogel fiber under single-cycle tensile test. The measured tensile strength is 3.0 MPa and Young's modulus is 1.6 MPa. **b,** Plot of crack extension rate vs. energy release rate of the hydrogel-silica interface under cyclic peeling test. The measured interfacial fatigue threshold is 625 J m^{-2}. **c,** Plot of strain vs. cycle number of the hydrogel fiber under cyclic tensile test. The applied stress amplitude in the cyclic tensile test is 1.4 MPa and the total cycle number (N_c) is larger than 10,000. **d,** Microscopic images of the hydrogel fiber at different tensile stresses under cyclic tensile test. Scale bars: 0.5 mm. **e-f,** Representative plots of stress vs. cycle number of the hydrogel fiber under cyclic tensile test before implantation (**e**) and after 8-week implantation (**f**). The applied strain amplitudes are 25%. **g,** Images of the hydrogel fiber (no cladding) at different tensile strains with two ends connected to a light source and a photodetector, respectively. Scale bars: 5 mm. **h,** Representative plots of strain and normalized light intensity vs. cycle number of the hydrogel fiber. **i,** Representative plot of normalized light intensity vs. tensile strain of the silica, PDMS, and hydrogel fibers in PBS. **j,** Comparison of the attenuation coefficient and Young's modulus of the hydrogel fiber and various transparent materials, including silica, PDMS, PMMA, PS, COC, and PC. **k,** Images of a porcine artery with no fiber showing free deformation, an artery with a silica fiber attached showing constrained deformation, and an artery with a hydrogel fiber attached showing free deformation. Scale bars: 10 mm.

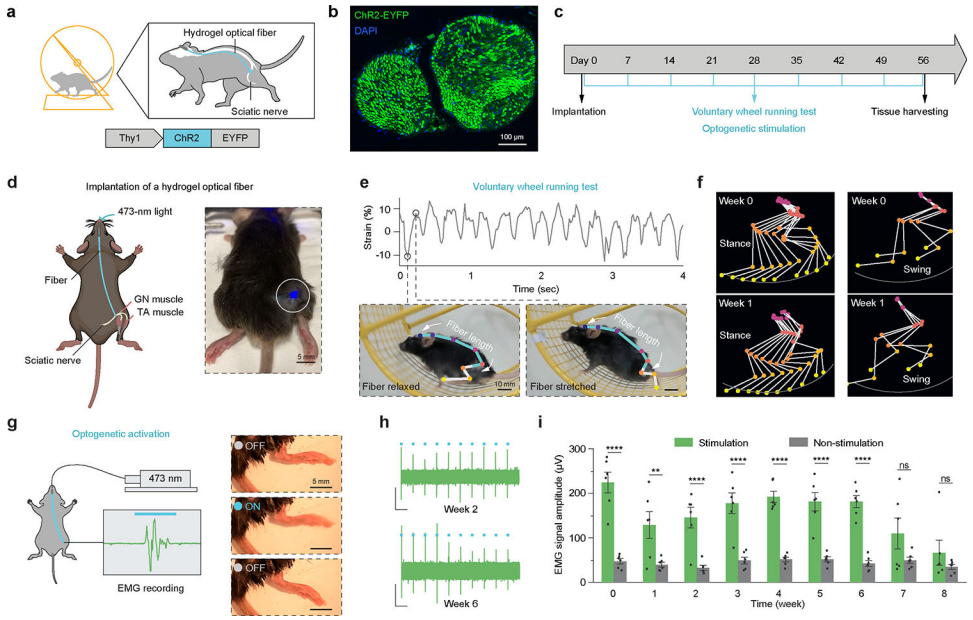

Figure 3. Optogenetic stimulation enabled by hydrogel optical fibers.

a, Schematic showing the optogenetic stimulation of hindlimb muscles with a hydrogel fiber in Thy1::ChR2-EYFP transgenic mice. **b,** Confocal image of sciatic nerve cross-section showing ChR2-EYFP expression. Scale bar: 100 μm. **c,** In vivo study design and timeline of implantation, voluntary wheel running test, optogenetic stimulation, and tissue harvesting over 8 weeks. **d,** Schematic and image showing a mouse implanted with a hydrogel optical fiber. Scale bar: 5 mm. **e,** Representative plot of the mechanical strain of the hydrogel fiber in a mouse over time during voluntary wheel running test. The bottom images show the pose estimation of a mouse implanted with a hydrogel fiber on a running wheel. The mouse is labeled with nodes for the ferrule, neck, back, iliac crest, hip, knee, ankle, and toe. The fiber length, highlighted in blue, is calculated by the total length of the segments starting from the ferrule to the middle point between the hip and knee. Scale bars: 10 mm. **f,** Kinematic stick diagram of mouse hindlimb movement on a running wheel on week 0 before and week 1 after implantation. A gait cycle is composed of a stance phase (left) and a swing phase (right) in the stick diagram. The nodes represent the iliac crest, hip, knee, ankle, and toe from top to bottom. **g,** Schematic showing the optogenetic stimulation controlled by optical pulses from a 473-nm light source and recorded by EMG. The left images show the ankle joint movement in response to optogenetic stimulation. Scale bars: 5 mm. **h,** Plots of EMG signals recorded on week 2 and week 6 after implantation. Blue bars indicate optical pulses with a pulse width of 10 ms and irradiance of 35.4 mW mm^{-2}. Scale bar, 1 s, 100 μV. **i,** Plot of EMG signal amplitude from week 0 before implantation to week 8 after implantation with and without optogenetic stimulation. ns: not significant.

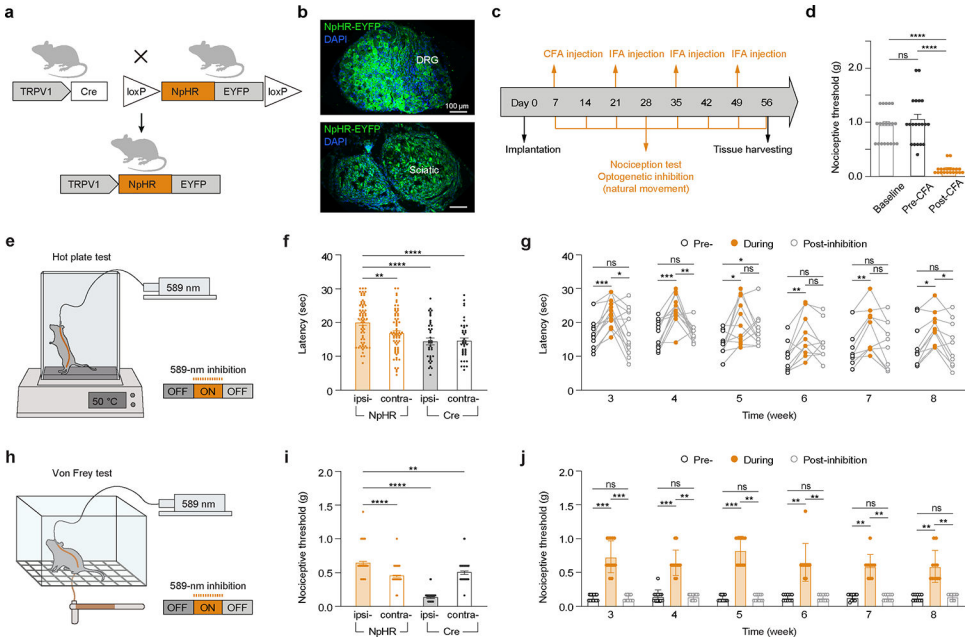

Figure 4. Optogenetic inhibition of nociception in naturally behaving mice enabled by hydrogel optical fibers.

a, Schematic of using a genetic cross to generate TRPV1::NpHR-EYFP transgenic mice that inhibitory opsins can be selectively expressed in TRPV1-lineage of DRG sensory neurons. **b,** Confocal images of DRG and sciatic nerve cross-sections showing NpHR-EYFP expression. Scale bar: 100 μm. **c,** In vivo study design and timeline of implantation, inducing inflammatory pain with CFA and IFA injection, nociception test, optogenetic inhibition, and tissue harvesting over 8 weeks. **d,** Nociceptive threshold of ipsilateral hind paw flinch before implantation (baseline), before CFA injection on day 6 post-implantation (pre-CFA), after CFA on day 7 post-implantation (post-CFA) to confirm the CFA-induced inflammation through von Frey tests. **e,** Schematic showing a mouse with a hydrogel optical fiber in hot plate tests. Optogenetic inhibition is controlled by optical pulses from a 589-nm laser source. Yellow bars indicate optical pulses with a pulse width of 25 ms and irradiance of 8.5 mW mm^{-2}. **f,** Latency of first-time ipsilateral and contralateral hind paw flinch during inhibition in evaluating thermal-nociceptive sensitivity through hot plate tests for TRPV1::NpHR-EYFP (test group) and TRPV1::Cre (control group) mice from week 3 to week 8. **g,** Latency of first-time ipsilateral hind paw flinch in hot plate tests for TRPV1::NpHR-EYFP mice over time after implantation. **h,** Schematic showing a mouse with a hydrogel optical fiber in von Frey tests. Optogenetic inhibition is controlled by optical pulses from a 589-nm light source. Yellow bars indicate optical pulses with a pulse width of 25 ms and irradiance of 8.5 mW mm^{-2}. **i,** Nociceptive threshold of ipsilateral and contralateral hind paw flinch during inhibition in evaluating mechanical allodynia through von Frey tests for TRPV1::NpHR-EYFP (test group) and TRPV1::Cre (control group) mice from week 3 to week 8. **j,** Nociceptive threshold of ipsilateral hind paw flinch in von Frey tests for TRPV1::NpHR-EYFP mice over time after implantation. ns: not significant.